The Astronomical Journal, 165:231 (19pp), 2023 June
https://doi.org/10.3847/1538-3881/acc074

Comprehensive Study of the Chemical Composition and Spatial Outgassing Behavior of Hyperactive Comet 46P/Wirtanen Using Near-IR Spectroscopy during its Historic 2018 Apparition

Younas Khan[1], Erika L. Gibb[1], Nathan X. Roth[2,3], Michael A. DiSanti[4,5], Neil Dello Russo[6], Boncho P. Bonev[7], Chemeda T. Ejeta[1], Mohammad Saki[8], Ronald J. Vervack, Jr.[6], Adam J. McKay[9], Hideyo Kawakita[10], Michael R. Combi[11], Danna Qasim[12], and Yinsi Shou[11]

[1] Department of Physics and Astronomy, University of Missouri-St. Louis, One University Boulevard, St. Louis, MO, USA; younas.khan@mail.umsl.edu
[2] Universities Space Research Association, Columbia, MD 21046, USA
[3] Solar System Exploration Division, Astrochemistry Laboratory Code 691 NASA Goddard Space Flight Center, Greenbelt, MD 20771 USA
[4] Solar System Exploration Division, Planetary Systems Laboratory, NASA Goddard Space Flight Center, Greenbelt, MD 20771, USA
[5] Goddard Center for Astrobiology, NASA Goddard Space Flight Center, Greenbelt, MD 20771, USA
[6] Space Exploration Sector, Johns Hopkins University Applied Physics Laboratory, Laurel, MD 20723, USA
[7] Department of Physics, American University, Washington, DC 20016, USA
[8] Physics Department, Leach Science Center, Auburn University, Auburn, AL, USA
[9] Department of Physics and Astronomy, Appalachian State University, Boone, NC 28608-2106, USA
[10] Koyama Astronomical Observatory, Kyoto Sangyo University, Motoyama, Kamigamo, Kita-ku, Kyoto 603-8555, Japan
[11] Department of Climate and Space Sciences and Engineering, University of Michigan, Ann Arbor, MI, USA
[12] Southwest Research Institute, San Antonio, TX 78238, USA

Received 2022 December 18; revised 2023 February 13; accepted 2023 February 26; published 2023 May 9

Abstract

We present a comprehensive analysis of the chemical composition of the Jupiter-family comet and potential spacecraft target 46P/Wirtanen, in the near-IR wavelength range. We used iSHELL at the NASA Infrared Telescope Facility to observe the comet on 11 pre-, near-, and postperihelion dates in 2018 December and 2019 January and February during its historic apparition. We report rotational temperatures, production rates, and mixing ratios with respect to H_2O and C_2H_6 or 3σ upper limits of the primary volatiles H_2O, HCN, CH_4, C_2H_6, CH_3OH, H_2CO, NH_3, CO, C_2H_2, and HC_3N. We also discuss the spatial outgassing of the primary volatiles, to understand their sources and the spatial associations between them. The spatial profiles of H_2O in 46P/Wirtanen suggest the presence of extended H_2O outgassing sources in the coma, similar to the EPOXI target comet 103P/Hartley 2. 46P/Wirtanen is among the few known hyperactive comets, and we note that its composition and outgassing behavior are similar to those of other hyperactive comets in many ways. We note that the analyzed parent volatiles showed different variations (relative mixing ratios) during the apparition. We compared the chemical composition of 46P/Wirtanen with the mean abundances in Jupiter-family comets and the comet population as measured with ground-based near-IR facilities to date. The molecular abundances in 46P/Wirtanen suggest that although they were changing, the variations were small compared to the range in the comet population, with CH_3OH showing notably more variation as compared to the other molecules.

Unified Astronomy Thesaurus concepts: Short period comets (1452); Comets (280); Comet volatiles (2162); Near infrared astronomy (1093); Comae (271); Molecular spectroscopy (2095)

Supporting material: figure set

1. Introduction

Comets are thought to preserve the compositional signatures of the regions in the early solar system where they formed ∼4.5 Gyr ago. For this reason, they are sometimes referred to as the "fossils" of our solar system. The characterization of comets provides fundamental insights into the processes that were involved in the formation and evolution of the early solar system (Mumma et al. 1993; Irvine et al. 2000; Bockelée-Morvan et al. 2004). Comets might also have contributed to ocean water (Gomes et al. 2005) and other organics on Earth, signifying their importance for understanding the emergence of life. Based on where they were stored in the solar system, comets are broadly categorized into two classes: (a) ecliptic comets, including Jupiter-family comets (JFCs), originate from the Kuiper Belt, just beyond Neptune's orbit, and are characterized by short orbital periods (<200 yr) and low angles of inclination with respect to the ecliptic plane; and (b) nearly isotropic comets (also referred to as Oort Cloud comets; or OCCs) that originate from the Oort cloud and have much longer orbital periods. The classical paradigm of the formation of comets suggests that OCCs formed in a region ∼5–30 au from the Sun, while ecliptic comets formed at distances >30 au, with the migration of the young giant planets (as proposed in the Nice model) gravitationally displacing the comets into their current reservoirs (Morbidelli & Brown 2004; Gladman 2005). However, recent dynamical models (Levison & Duncan 1997; Gomes et al. 2005; Morbidelli et al. 2005; Levison et al. 2011; Nesvorný et al. 2017) and the presence of crystalline silicates in comets of both dynamical classes—such as C/2001 Q4 (NEAT; Wooden et al. 2004), 1P/Halley (Bregman et al. 1987), 9P/Tempel 1 (Harker et al. 2005), and 81P/Wild 2 (Zolensky et al. 2006)—suggest that JFCs and OCCs might actually have formed in (or at least incorporated materials from) a large overlapping region between 5 and 30 au from the Sun, with the JFCs probably forming closer to the Sun than the OCCs, on average. A comparison of the observed compositions of ∼30 comets with predictions from protostellar disk models suggests that while the models can account for the observed ranges in the mixing ratios of each molecule, no single location or time can reproduce the abundances simultaneously, implying that comets consist of materials that are processed under a variety of conditions (Willacy et al. 2022). These processed materials might have experienced radial or vertical transport, before being incorporated into comets. Comparisons of these models with the average OCC and JFC compositions also suggest that the two classes of comets likely formed in overlapping regions, as discussed above.

Comets consist of ices of a variety of molecules (dominated by H_2O) and dust. When a comet enters the inner solar system, radiation from the Sun starts to sublimate the ices, resulting in an extended and freely expanding envelope of gas (the coma) and dust from the nucleus. Ground-based near-IR spectroscopy is a powerful tool for characterizing the primary volatiles—the molecules that are directly sublimated from a comet's nucleus into its coma— by sampling the rovibrational transitions of a suite of molecules between ∼2.9 and 5 μm. The primary volatile compositions of comets as obtained using near-IR spectroscopy are assumed to closely mirror the composition within the nucleus when a comet approaches close enough to the Sun for sublimation of all the measured volatiles (particularly H_2O, the least volatile ice measured) to be uninhibited (generally within ∼2 au). In contrast, tracing the lineage of daughter/granddaughter species that are characterized at optical wavelengths, to infer the primary volatile composition, is more challenging, owing to the complex coma chemistry that is present, including multiple potential progenitor materials (both volatile and refractory) that may be associated with a given daughter/granddaughter species.

Individual comets have diverse dynamical histories, but OCCs and JFCs also experience distinct processing histories, on average, owing to their significantly different orbital periods and number of close perihelion passages, both of which could plausibly impact their present-day compositions. If postformation thermal processing effects dominate in comets, we expect JFCs to be relatively depleted in more volatile ices, owing to their frequent passages close to the Sun as compared to OCCs. In contrast, if cosmogonic/natal effects are dominant, JFCs and OCCs should have similar compositions, if they formed in chemically overlapping regions, or different compositions, if they formed in regions having distinct chemistries. Cometary scientists have been striving to resolve fundamentally important questions, including but not limited to the following.

1. To what extent do comets represent the chemical composition of the early solar system?
2. Are the chemical compositions of comets dominated by primordial effects or by postformation processing?
3. Are there any systematic differences between the compositions of comets originating from different reservoirs?
4. How are the ices of different molecules associated with each other in the nucleus?
5. Does the composition of comets from different reservoirs reflect distinct or overlapping formation regions?

To date, the primary volatile compositions of ∼50 comets have been characterized in the near-IR, with only ∼15 of those being JFCs. In general, there is chemical diversity among comets from each dynamical class, as well as among the overall population. Moreover, on average, JFCs are depleted in some primary volatiles (especially in the hypervolatiles CO, CH_4, and C_2H_6) as compared to OCCs (Dello Russo et al. 2016). While this depletion is consistent with evolutionary volatile loss through the more intense thermal processing of JFCs, various sources of observational evidence point to cosmogonic effects (the formation region and conditions) as being the most likely reason for these differences. For example, more than 200 comets that have been measured at optical wavelengths for a few daughter/granddaughter species (A'Hearn et al. 1995; Fink 2009; Cochran et al. 2012; Schleicher & Bair 2014) reveal that the depletion of carbon-chain species shows no correlation to dynamical age, suggesting that the compositional differences between the two dynamical classes are likely natal, rather than due to postformation processing (A'Hearn et al. 1995; Schleicher 2007; Dello Russo et al. 2009; Fink 2009). Additional evidence for the retention of primordial chemistry in comets is provided by the similarity in composition of the two fragments of JFC 73P/Schwassmann–Wachmann 3 (Dello Russo et al. 2007). Our understanding of the chemical compositions of the primary volatiles in comets has improved significantly over recent years, largely owing to advancements in near-IR instrumentation, combined with highly favorable apparitions of multiple JFCs. Nonetheless, a sufficiently larger sample of comets from both dynamical reservoirs needs to be studied, to achieve a more complete understanding and to develop a robust cometary taxonomy based on primary volatiles.

Some comets have displayed variations in their primary volatile composition at different heliocentric distances (R_h), due to seasonal effects (e.g., post versus preperihelion asymmetries) or owing to nucleus rotation (diurnal effects; Luspay-Kuti et al. 2015; Roth et al. 2018). These observed variations in abundances suggest spatially variable compositions within the nuclei of at least some comets. This calls for serial observing campaigns, ideally spanning a wide range of R_h and encompassing different cometary seasons. However, to date, the volatile compositions of relatively few comets have been observed over a range of R_h and/or both pre- and postperihelion during a given apparition. This results in the so-called "snapshot bias," i.e., observations of a comet at a single R_h, or over a limited range of R_h, which complicates the interpretation of its composition and outgassing behavior. In this work, we present the most comprehensive compositional analysis to date of the JFC 46P/Wirtanen (hereafter, 46P), which was observed on 11 dates spanning approximately two months. The heliocentric distance ranged between ∼1.06–1.27 au over this period, and we sampled the comet on one preperihelion date and multiple near- and postperihelion dates, with the goal of addressing this snapshot bias.

1.1. Comet 46P and Its Historic 2018 Apparition

46P is a JFC with an orbital period of 5.4 yr and a rotation period of ∼9 hr (Jehin et al. 2018; Farnham et al. 2018; Moulane et al. 2019). 46P's historic apparition over 2018–19 led to a worldwide observing campaign that attracted the attention of astronomers.[13] 46P reached its perihelion on UT 2018 December 12, with an R_h of ∼1.05 au. It reached a

---

[13] http://wirtanen.astro.umd.edu

minimum geocentric distance (Δ) of 0.077 au (∼30 lunar distances) and a visual magnitude of ∼3 on 2018 December 16, resulting in unprecedented observing circumstances for a JFC. The 2018 apparition of 46P was the most favorable on record, and its distance of closest approach is among the top 20 for a comet over the last 200 yr.[14] Comet 46P remained within 0.1 au from Earth for ∼three weeks, allowing for detailed observations at various wavelengths, which resulted in high-quality scientific data.

Production rates and mixing ratios (also called abundances) were determined for the primary volatiles H_2O, HCN (hydrogen cyanide), CH_4 (methane), C_2H_6 (ethane), CH_3OH (methanol), H_2CO (formaldehyde), NH_3 (ammonia), CO (carbon monoxide), C_2H_2 (acetylene), and HC_3N (cyanoacetylene). This comprehensive characterization of a JFC will add important measurements to the developing chemical taxonomy of comets. Moreover, 46P was the original target of the Rosetta mission (before a delay in the launch resulted in sending the spacecraft to comet 67P/Churyumov–Gerasimenko; hereafter, 67P/CG), and it remains a favorable spacecraft target. As such, knowledge of its composition, activity, and spatial outgassing behavior is important for characterization, prior to a future mission encounter. The 2018 apparition was especially favorable for studying the spatial outgassing behavior and association of primary volatiles. The small geocentric distance permitted sampling of the innermost coma of 46P, which is among the few comets to have shown hyperactive behavior (Combi et al. 2019).

In Sections 2 and 3, we discuss our observations and the data reduction procedures, respectively. In Section 4, we present our results, then discuss them by comparing them with the results from other comets observed in the near-IR, as well as at other wavelengths.

2. Observations

We observed 46P using the iSHELL spectrograph at the 3 m NASA Infrared Telescope Facility (IRTF; Rayner et al. 2012, 2016) on 11 UT dates between 2018 December 6 and 2019 February 5 (see Table 1 for the observing details). The iSHELL at the IRTF is excellent for comet studies, owing to its cross-dispersed capability (leading to extensive spectral coverage per setting), its excellent sensitivity in the 1.1–5.3 μm range, where many parent volatiles have strong vibrational bands, its high spectral resolution ($\lambda/\Delta\lambda$) of $\sim 4 \times 10^4$, with the 0.″75 (6 pixel) wide slit, and its spatial coverage over the 15″ length of the slit. For all observations, we used "on-chip" nodding to acquire the comet data, with the standard A–B–B–A image sequence. In this sequence, the A and B beam positions are placed symmetrically with respect to the slit's center, and are separated by half its length (i.e., by 7.″5). For the flux calibration, we observed a bright nearby standard star, using the 4″ wide slit with each iSHELL setting. Using a wider slit for observing the standard star results in a lower resolving power, but it helps to minimize the slit losses, leading to lower uncertainty in the flux calibration.

3. Data Reduction

The data reduction techniques that are used in this work are described in detail in the literature (Bonev 2005; DiSanti et al. 2006, 2014; Villanueva et al. 2009; Radeva et al. 2010; DiSanti et al. 2017). The spectra were combined as A–B–B+A; this canceled continuum emissions from the thermal background, sky lines and continuum, and instrumental biases, resulting in frames having a net comet signal in the A and B positions. We applied dark-subtracted flats to the data, which were subsequently cleaned of hot pixels and cosmic-ray hits. We straightened the frames and obtained 2D spatial–spectral arrays, with each row corresponding to a unique spatial position along the slit and each column representing a unique wavelength. To account for the possible drifting of the comet along the slit during the acquisition of multiple frames, we registered the signals within each A and B beam to a common spatial position. After combining the signals from the summed A and B beams, spectra were extracted by summing the signal over 15 rows (∼2.″5), seven rows to each side of the dust continuum.

Figures 1(A)–(D) show the emission spectra of the primary volatiles on UT 2018 December 14. We determined the contributions from the continuum and gaseous emissions in our spectra following the process that has previously been described by DiSanti et al. (2016). We used the Planetary Spectrum Generator[15] (Villanueva et al. 2018) to obtain telluric transmittance models, to perform wavelength calibration of the spectra, and to determine the column burdens of the absorbing molecules in the terrestrial atmosphere. The fully resolved transmittance function was convolved to the resolving power ($\sim 4 \times 10^4$) of the instrument, and scaled to the continuum level of the comet. The telluric model was then subtracted from the observed spectrum, to isolate cometary emission lines. The intensities of these emission lines were compared to fluorescent emission models, after correcting each modeled line intensity for the monochromatic atmospheric transmittance at its Doppler-shifted wavelength, based on the geocentric velocity of the comet.

The temperature-dependent fluorescence efficiencies (g-factors; photons s^{-1} molecule^{-1}) that have been used in this work were generated with quantum mechanical models developed for H_2O (Villanueva et al. 2012b), C_2H_6 (Villanueva et al. 2011b), CH_3OH (Villanueva et al. 2012a; DiSanti et al. 2013), CH_4 (Gibb et al. 2003), CO (DiSanti et al. 2001; Paganini et al. 2013), H_2CO (DiSanti et al. 2006), C_2H_2 (Villanueva et al. 2011a), NH_3 (Villanueva et al. 2013), and HCN (Lippi et al. 2013). HC_3N is a simple linear molecule, and its g-factors were obtained using a rotational constant of 0.15174 cm^{-1} (Creswell et al. 1977). To fit the fluorescent emissions from all molecules simultaneously in each echelle order, a Levenberg–Marquardt nonlinear minimization technique (Villanueva et al. 2008) was used. This technique allows for results with high precision, even in spectrally crowded regions with many lines from multiple molecules within a single resolution element of the instrument. In general, the rotational temperatures (T_{rot}) derived using this technique were consistent with the line-by-line analyses. Constraining T_{rot} was necessary for the accurate determination of the molecular production rates, and hence the mixing ratios, because the fluxes of the individual rovibrational lines were temperature-dependent. We determined T_{rot} using correlation and excitation analyses (Bonev 2005; DiSanti et al. 2006; Bonev et al. 2008).

---

[14] https://wirtanen.astro.umd.edu/close_approaches.shtml

[15] https://psg.gsfc.nasa.gov/

Table 1
[a] Observing Log for 46P during its 2018 Apparition

iSHELL Setting	Slit PA (°)	Standard Star	Time (UT)	R_h(au)	Δ (au)	Δ-dot (km s^{-1})	T_{int}(min)
			2018 December 6				
L-Custom	41	BS 8709	6:19–8:03	1.059	0.098	−6.4	92
Lp1	″	″	08:05–8:51	″	″	″	40
			2018 December 14				
Lp1	66	BS 2421	04:45–6:20	1.055	0.078	−1.8	84
L-Custom	″	″	6:26–8:58	″	″	″	138
M2	″	″	9:05–11:42	″	″	″	122
			2018 December 16				
L3-Custom	81	BS 2421	5:32–7:55	1.056	0.077	−0.2	116
L-Custom	″	″	8:06–9:54	″	″	″	96
Lp1-Custom	″	″	9:56–11:44	″	″	″	94
			2018 December 18				
L-Custom	102	BS 2421	09:42–10:04	1.058	0.078	1.7	18
L3-Custom	″	″	10:09–11:53	″	″	″	96
			2018 December 19[b]				
M2	113	BS 8781	5:47–8:13	1.058	0.079	2.3	114
L-Custom	113	″	8:17–9:34	″	″	″	68
Lp1	113	″	9:47–11:16	″	″	″	76
Lp1	23	″	11:20–12:38	″	″	″	68
			2018 December 21[c]				
Lp1	134	BS 8781	5:45–6:02	1.061	0.082	3.7	16
L-Custom	134	″	6:10–7:29	″	″	″	72
L-Custom	44	″	7:43–8:52	″	″	″	64
L-Custom	134	″	8:57–10:07	″	″	″	64
L-Custom	44	″	10:21–11:55	″	″	″	84
			2019 January 11				
M2	203	BS 4905	9:29–11:51	1.13	0.18	+10.1	107
Lp1	″	″	11:53–14:03	″	″	″	116
L-Custom	″	″	14:13–15:14	″	″	″	52
			2019 January 12				
Lp1	203	BS 4905	9:39–11:51	1.13	0.18	+10.3	116
M2	″	″	11:52–13:48	″	″	″	136
			2019 January 13				
M2	203	BS 4905	9:28–11:04	1.14	0.19	+10.4	74
L-Custom	″	″	11:06–13:04	″	″	″	104
Lp1	″	″	13:10–14:04	″	″	″	48
			2019 February 4				
M2	187	BS 4357	9:37–11:36	1.27	0.33	+13.2	82
Lp1	″	″	11:39–13:09	″	″	″	72
			2019 February 5				
Lp1	185	BS 4357	9:42–10:57	1.28	0.33	+13.3	60

Notes.

[a] The wavelength ranges (in μm) spanned by the different iSHELL settings used in this work are as follows: L-Custom: 2.81–3.09; Lp1: 3.28–3.66; Lp1-Custom: 3.41–3.80; M2: 4.52–5.25; and L3-Custom: 3.16–3.44. "PA": position angle of the slit. "R_h": heliocentric distance. "Δ": geocentric distance. "Δ-dot": geocentric velocity (values correspond to the middle of the observing runs). "T_{int}": on-source integration time.

[b] On 2018 December 19, we sampled the comet twice using the Lp1 setting: first, we oriented the slit along the Sun–comet line (a PA of 113°), then we oriented it perpendicular to the Sun–comet line (a PA of 23°), to sample a different projection of the coma.

[c] On 2018 December 21, we alternated the PA between 134° and 44°, to obtain four data sets in the L-Custom setting, to sample different projections of the coma and to test any short-term variability in production rates.

Table 2 shows the rotational temperatures calculated for different species on different dates. Our derived rotational temperatures for the different molecules either agreed within uncertainty or were very close to one another on a given date. For the weaker species (C_2H_2, NH_3, H_2CO, CH_4, CO, and HC_3N), we could not obtain well-constrained T_{rot} values, therefore we assumed the T_{rot} as obtained from comeasured species. In general, the rotational temperatures that are calculated for different molecules using IR observations are consistent; moreover, small variations in T_{rot} only result in minor differences in production rates (Gibb et al. 2012), and hence mixing ratios.

The nucleocentric production rates (Q_{nc}) were determined using the well-documented Q-curve method (Dello Russo et al. 1998; DiSanti et al. 2001; Bonev 2005; Villanueva et al. 2011b; Gibb et al. 2012); see Section 3.2.2 of DiSanti et al. (2016) for further details. The Q_{nc} values are scaled by a multiplicative growth factor (GF), to establish the total (or global) production rates (Q; measured in molecules s^{-1}). The GF of a particular molecule is indicative of how the molecular flux is distributed along the slit, and it is defined as the ratio of the global and nucleocentric production rates (i.e., GF $= \frac{Q}{Q_{nc}}$). The Q-curve formalism corrects for atmospheric seeing, which

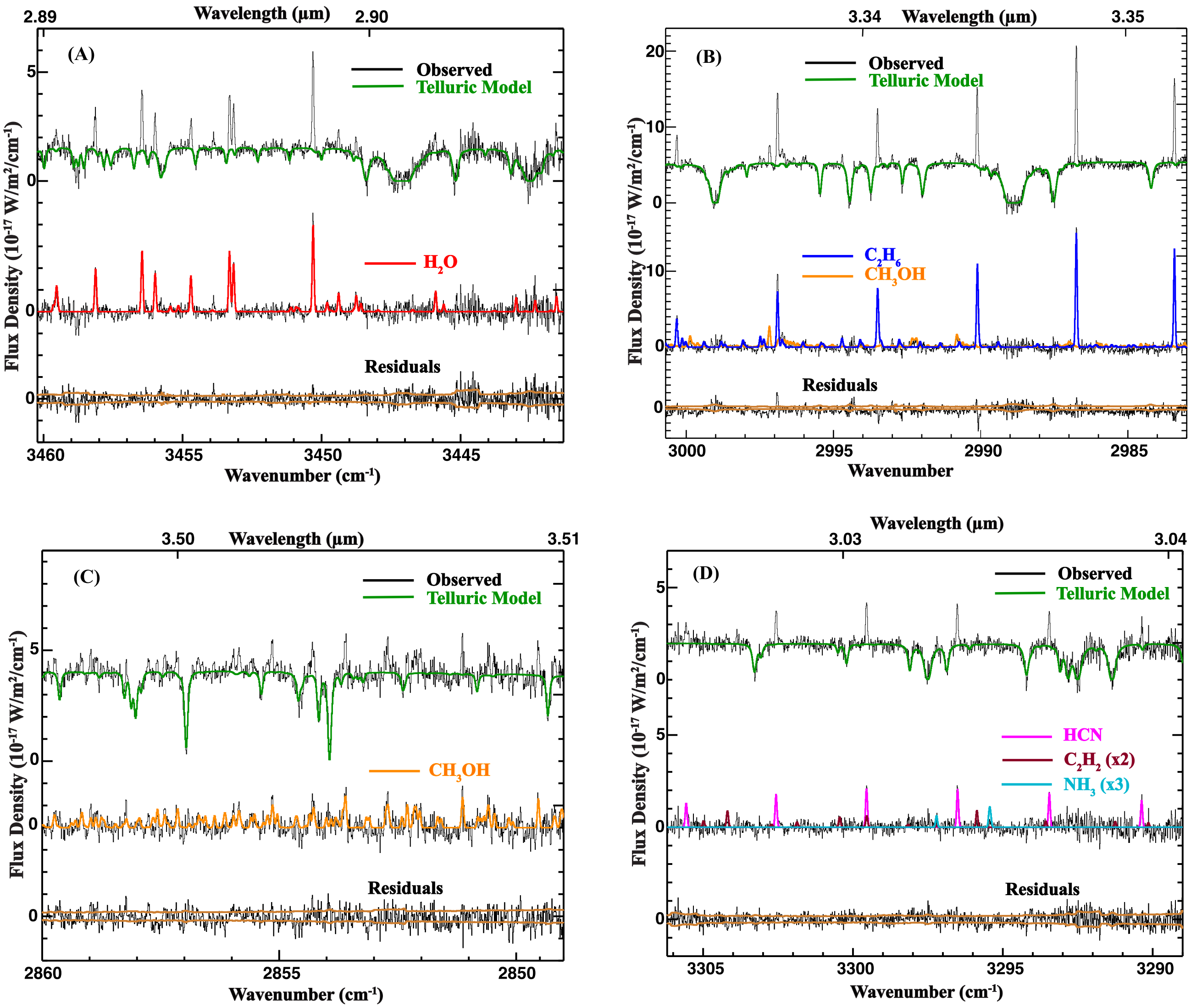

Figure 1. (A)–(D) Fluorescent emission spectra of the primary volatiles in 46P on a representative date (UT 2018 December 14). In each of these panels, the observed spectrum (black; at the top of the panel) is overplotted with the best-fit atmospheric absorption model (green). In the middle of each panel, synthetic models of molecular emissions (color-coded) are combined and overplotted on the cometary spectrum, after subtracting the modeled atmospheric absorptions. The bottom of each panel shows the residual spectrum, with the ±1σ uncertainty envelope in brown. Lines corresponding to the weaker species NH_3 and C_2H_2 have been multiplied by a factor for visual clarity.

(The complete figure set (four images) is available.)

suppresses the signal along lines of sight passing close to the nucleus, owing to the use of a narrow slit, as well as the potential drift of the comet across the slit during an exposure sequence. The production rates for each primary volatile were then determined from the corresponding synthetic model at a well-constrained $T_{\rm rot}$. The mixing ratio with respect to the H_2O of a primary volatile is defined as the ratio of the global production rate of the molecule to that of the H_2O (i.e., the mixing ratio of molecule $X = Q_{\rm x}/Q_{\rm H2O}$). The GFs, Qs, and mixing ratios (with respect to H_2O and C_2H_6) obtained in this work are listed in Table 2.

4. Results and Discussion

4.1. Molecular Emission Spectra

Panels (A) to (D) of Figure 1 show the spectra for 46P with detections of H_2O, C_2H_2, HCN, NH_3 (all sampled in the L-Custom iSHELL setting) and CH_3OH and C_2H_6 (sampled in the Lp1 setting), for UT 2018 December 14. In each of these panels, the observed spectrum (black) is shown at the top, with the synthetic telluric model overplotted (green). Directly below, the individual fluorescent models (color-coded) are overplotted on top of the observed spectra, after the telluric models have been subtracted. The bottoms of each panel show the "residual" noise after subtracting the synthetic models. The brown envelope represents the (±1σ) uncertainty. Most of the photon noise is encompassed by the ±1σ envelope, indicating the quality of our data and the robust implementation of the data reduction process. For the spectral galleries corresponding to UT 2018 December 18 and 21 and 2019 January 11–13 and February 4–5, see Roth et al. (2021a), Khan et al. (2021), McKay et al. (2021), and Saki (2021), respectively. The spectral galleries for 2018 December 6, 16, and 19 are presented in the Figure Set for Figure 1.

Table 2
Production Rates and Mixing Ratios of the Primary Volatiles Sampled in 46P

Molecule	GF[a]	$T_{\rm rot}$[b]	Q (10^{25} mol s^{-1})[c]	Mixing Ratio[d]	
				$H_2O = 100$	$C_2H_6 = 1.00$
			2018 December 6		
H_2O	2.22 ± 0.07	85 ± 1	618 ± 27.5	100	90.8 ± 5
HCN	2.1 ± 0.06	81^{+5}_{-4}	1.24 ± 0.07	0.20 ± 0.01	0.18 ± 0.01
C_2H_2	(2.22)	(85)	0.75 ± 0.06	0.12 ± 0.01	0.11 ± 0.01
C_2H_2	(2.1)	(81)	0.7 ± 0.05	0.11 ± 0.01	0.10 ± 0.01
NH_3	(2.22)	(85)	6.89 ± 1.26	1.11 ± 0.2	1.01 ± 0.19
CH_3OH	2.3 ± 0.08	73 ± 5	21.9 ± 1.3	3.55 ± 0.26	3.23 ± 0.2
C_2H_6	2.21 ± 0.03	72 ± 3	6.8 ± 0.21	1.10 ± 0.06	1.00
H_2CO	(2.3)	(73)	<0.76	<0.12	<0.11
			2018 December 14		
H_2O	2.46 ± 0.07	84 ± 1	546 ± 22	100	89.05 ± 4.6
HCN	2.36 ± 0.15	80 ± 3	1.16 ± 0.09	0.21 ± 0.02	0.19 ± 0.02
C_2H_2	(2.36)	(80)	0.43 ± 0.05	0.08 ± 0.01	0.08 ± 0.01
C_2H_2	(2.46)	(84)	0.46 ± 0.08	0.09 ± 0.01	0.08 ± 0.01
NH_3	(2.46)	(84)	3.69 ± 0.6	0.67 ± 0.08	0.60 ± 0.1
CH_3OH	2.55 ± 0.2	71 ± 4	17.6 ± 1.6	3.22 ± 0.22	2.87 ± 0.25
C_2H_6	2.14 ± 0.02	75 ± 3	6.13 ± 0.2	1.12 ± 0.06	1.00
H_2CO	(2.55)	(71)	<0.42	<0.08	<0.07
			2018 December 16		
H_2O	2.5 ± 0.1	80 ± 1	818 ± 33	100	135 ± 15
HCN	2.6 ± 0.3	81 ± 4	1.8 ± 0.1	0.22 ± 0.02	0.30 ± 0.04
C_2H_2	(2.6)	(80)	0.9 ± 0.1	0.11 ± 0.02	0.15 ± 0.03
NH3	(2.6)	(80)	4.1 ± 0.60	0.49 ± 0.08	0.7 ± 0.1
CH_3OH[e]	2.8 ± 0.3	(70)	22 ± 2	2.7 ± 0.3	3.7 ± 0.3
CH_3OH[f]	2.7 ± 0.1	70 ± 3	24 ± 3	3 ± 0.5	4.0 ± 0.7
C_2H_6	2.6 ± 0.1	68 ± 2	6.1 ± 0.2	0.74 ± 0.08	1.00
H_2CO	(2.7)	(70)	<1	<0.13	<0.2
			2018 December 18[g]		
H_2O	2.4 ± 0.2	94 ± 5	825 ± 60	100	131 ± 14
CH_3OH	2.3 ± 0.1	88^{+18}_{-15}	22 ± 2	2.8 ± 0.3	3.5 ± 0.2
C_2H_6	2.05 ± 0.04	90 ± 3	6.3 ± 0.2	0.75 ± 0.08	1.00
			2018 December 19		
H_2O	2.72 ± 0.15	83 ± 2	719 ± 48	100	96 ± 10
HCN	2.77 ± 0.1	71^{+6}_{-5}	1.4 ± 0.11	0.19 ± 0.02	0.17 ± 0.02
C_2H_2	(2.72)	(83)	0.84 ± 0.16	0.12 ± 0.02	0.10 ± 0.02
NH_3	(2.72)	(83)	5.14 ± 1.15	0.71 ± 0.08	0.62 ± 0.15
CH_3OH[h]	3.07 ± 0.1	62 ± 3	25.3 ± 1.66	3.52 ± 0.39	3.05 ± 0.21
CH_3OH[i]	3.14 ± 0.14	69^{+5}_{-4}	26.2 ± 2	3.64 ± 0.4	3.05 ± 0.31
C_2H_6[h]	2.6 ± 0.08	60 ± 2	7.5 ± 0.44	1.04 ± 0.11	1.00
C_2H_6[i]	3.15 ± 0.22	67 ± 2	7.99 ± 0.71	1.11 ± 0.15	1.00
H_2CO	(3.07)	(83)	0.67 ± 0.17	0.09 ± 0.03	0.09 ± 0.02
			2018 December 21[j]		
H_2O	2.20	81 ± 2	584 ± 29	100	141 ± 15
HCN	2.30	80 ± 2	1.32 ± 0.08	0.23 ± 0.02	0.32 ± 0.03
C_2H_2	(2.20)	(80)	0.46 ± 0.04	0.08 ± 0.01	0.11 ± 0.02
NH_3	(2.20)	(80)	2.91 ± 0.35	0.50 ± 0.06	0.71 ± 0.12
HC3N	(2.20)	(80)	<0.04	<0.007	<0.01
CH_3OH	2.40 ± 0.09	(80)	24.9 ± 1.6	4.26 ± 0.34	6.03 ± 0.75
C_2H_6	1.64 ± 0.04	(80)	4.12 ± 0.5	0.71 ± 0.09	1.00
H_2CO	(2.40)	(80)	<0.78	<0.13	<0.19
			2019 January 11[k]		
H_2O[l]	1.61 ± 0.05	(67)	570 ± 43	100	148 ± 14
H_2O[m]	1.70 ± 0.10	72 ± 6	412 ± 32	100	108 ± 11
HCN	(1.70)	(72)	1.34 ± 0.26	0.32 ± 0.07	0.35 ± 0.07
CH_3OH	(1.54)	(67)	12.5 ± 0.79	2.19 ± 0.22	3.24 ± 0.10
C_2H_6	1.54 ± 0.04	67 ± 2	3.85 ± 0.22	0.68 ± 0.06	1.00
CH_4	(1.54)	(67)	<5.55	<0.97	<1.44
CO	(1.61)	(67)	<3.09	<0.54	<0.82
			2019 January 12[k]		
H_2O	1.52 ± 0.15	(73)	389 ± 44	100	99 ± 13
CH_3OH	(1.67)	(73)	12.0 ± 0.8	3.08 ± 0.41	3.04 ± 0.11
C_2H_6	1.67 ± 0.05	73 ± 2	3.94 ± 0.23	1.01 ± 0.13	1.00
CH_4	(1.67)	(73)	<6.11	<1.57	<1.55

Table 2
(Continued)

Molecule	GF[a]	$T_{\rm rot}$[b]	Q (10^{25} mol s^{-1})[c]	Mixing Ratio[d]	
				$H_2O = 100$	$C_2H_6 = 1.00$
CO	(1.52)	(73)	<3.24	<0.84	<0.92
2019 January 13[k]					
H_2O[l]	1.51 ± 0.12	(66)	352 ± 44	100	83 ± 13
H_2O[m]	1.54 ± 0.04	66 ± 4	425 ± 22	100	100 ± 9
HCN	(1.54)	(66)	0.65 ± 0.07	0.15 ± 0.02	0.15 ± 0.02
CH_3OH	(1.76)	(66)	13.9 ± 1.4	3.27 ± 0.37	3.27 ± 0.17
C_2H_6	1.76 ± 0.13	66 ± 3	4.26 ± 0.39	1.00 ± 0.09	1.00
CH_4	(1.76)	(66)	<14.0	<3.29	<3.31
CO	(1.51)	(66)	<3.25	<0.92	<0.76
2019 February 4[n]					
H_2O	2.10 ± 0.20	59 ± 10	264 ± 34	100	118 ± 20
CH_3OH	(1.95)	(59)	3.01 ± 0.64	1.14 ± 0.30	1.34 ± 0.32
C_2H_6	1.95 ± 0.15	59 ± 7	2.23 ± 0.10	0.84 ± 0.14	1.00
CH_4	(1.95)	(59)	<0.84	<0.95	<1.13
CO	(2.14)	(59)	<1.49	<1.69	<2.00
H_2CO	(1.95)	(59)	<0.53	<0.60	<0.71
2019 February 5[n]					
CH_3OH	(1.95)	(59)	<1.55	<1.76	<2.08
CH_4	(1.95)	(59)	<2.75	<3.12	<3.69
H_2CO	(1.95)	(59)	<0.76	<0.86	<1.02

Notes.

[a] The growth factor: the ratio of the global and nucleocentered production rates. For the volatiles with weaker emission lines, the GFs of comeasured molecules were assumed (shown in parentheses).

[b] The rotational temperature: the values in parentheses are assumed, and correspond to comeasured molecules with well-constrained $T_{\rm rot}$.

[c] The global production rate. The uncertainties in the production rates include line-by-line deviations between the observed and modeled intensities and photon noise (see Dello Russo et al. 2004; Bonev 2005; Bonev et al. 2007). They also include the uncertainties in the GFs and flux calibrations, which were determined by calculating the standard deviations of gammas from eight exposures. Where possible, lines from multiple orders were coadded, to obtain production rates with higher signal-to-noise ratios.

[d] The mixing ratios: the ratios of the production rates with respect to H_2O (in percent) and with respect to C_2H_6 (as fractions).

[e] From the L3-Custom setting.

[f] From the Lp1-Custom setting.

[g] Roth et al. (2021a).

[h] Corresponding to a PA of 113°.

[i] Corresponding to a PA of 23°.

[j] Khan et al. (2021).

[k] McKay et al. (2021; except the HCN values).

[l] From the M2 setting.

[m] From the L-Custom setting.

[n] Saki (2021).

4.2. Spatial Distribution of Primary Volatiles

The spatial distribution of the gases in a coma is indicative of their outgassing sources and associations (or lack thereof) among different ices in the cometary nucleus. Additionally, it might also have implications for understanding the hyperactivity of a comet such as 46P. In general, a gas sublimating directly from the nucleus is characterized by a spatial profile peaked at the nucleus that falls off roughly as 1/r, where r is the distance from the nucleus (assuming a spherically symmetric uniform outflow). Conversely, outgassing from additional sources (such as icy grains/chunks ejected from the nucleus and sublimating in the coma) generally exhibit broader profiles, which fall off more slowly with distance from the nucleus. Solar photons can break more complex molecules into simpler species—e.g., H_2CO and NH_2—which also generally show broader profiles. Comparisons of simultaneously (or near-simultaneously) measured gas (and dust) profiles can indicate whether the gases are sublimating from one or more sources in the coma and whether individual molecular species have similar or distinct outgassing patterns.

Leveraging the long-slit spectroscopy afforded by iSHELL, 46P's near naked-eye brightness, and the small geocentric distance on most of the observing dates has enabled us to sample the spatial distribution of multiple primary volatiles in the inner coma (within a few hundred kilometers) on multiple dates. It is rare to sample the spatial distributions of primary volatiles in this range of distances from the nucleus—a transitional region between what could be observed with in situ cometary missions and what is more typically measured from ground-based telescopes. In Figures 2–3, we show the spatial profiles of simultaneously measured gases and dust, overplotted on top of one another, corresponding to 2018 December 6, 14, 16, and 19. The profiles are overplotted such that the origin coincides with the peak of the dust profiles. On 2018 December 19, we aligned the slit parallel to the Sun–comet line (a position angle, or PA, of 113°) as well as perpendicular to the Sun–comet line (a PA of 23°) for the Lp1 setting (see Table 1). The spatial profiles corresponding to these mutually perpendicular slit orientations are shown in panels (A) and (B) of Figure 3. The profiles were normalized to the intensity of the molecule with the highest peak emission.

4.2.1. H_2O and HCN

The H_2O spatial profiles showed similar features on 2018 December 6 (preperihelion), 14, and 19 (postperihelion; Figures 2–3), when compared to the corresponding dust profiles. On these dates, the profiles were broader than the comeasured dust profiles, and they were clearly enhanced antisunward; however, the profiles corresponding to the postperihelion dates were slightly different than that corresponding to the preperihelion date, in that the enhancements were more pronounced on the postperihelion dates. Also, the enhancements in the gas profiles with respect to dust became evident closer to the nucleus on the postperihelion dates, as compared to the preperihelion date, on which the enhancements became noticeable beyond ∼50 km from the nucleus. H_2O generally exhibited spatial profiles that were preferentially enhanced in one direction on other dates, too, which might be indicative of extended sources of outgassing (e.g., icy grains in the coma). For example, on 2018 December 18, the H_2O spatial profile was broader than the comeasured dust continuum, and it also showed antisunward enhancement (see Figure 3 in Roth et al. 2021a), possibly due to icy grains of H_2O being driven antisunward by the radiation pressure. A direct comparison with the spatial profiles from contemporaneous yet independent measurements that were obtained with the upgraded Keck/NIRSPEC (Bonev et al. 2021) on 2018 December 17 and 18 showed excellent agreement with the spatial profiles obtained with iSHELL (see Figures 6 and 7 in Roth et al. 2021a). We note that, given its larger spatial coverage, the NIRSPEC measurements further tested the presence of H_2O icy grains through rotational temperature analysis at different distances from the nucleus. On 2018 December 21, we extracted four H_2O spatial profiles (corresponding to the four sets of data obtained using the L-Custom iSHELL setting in two mutually perpendicular slit orientations) and obtained results that were similar to our 2018 December 18 results—i.e., a broader H_2O profile with antisunward enhancement (see Figure 2 in Khan et al. 2021). Our iSHELL results, nearly three weeks later (2019 January 11–13), also showed tentative evidence of H_2O enhancements antisunward (Figure 1 in McKay et al. 2021). Overall, these preferential enhancements in the antisunward direction are also consistent with the A'Hearn model of hyperactivity (A'Hearn et al. 2011), which predicts that icy grains ejected into the coma are pushed antisunward by the solar wind, with these grains acting as secondary sources of outgassing in the coma. In 2019 January, however, we note that an increase in the geocentric distance degraded the spatial resolution of these observations relative to earlier measurements, making it more difficult to discern H_2O antisunward enhancement as compared to the more pronounced enhancements seen in 2018 December. The spatial distribution of water in 46P and the presence of extended sources of outgassing in its coma have important implications for its hyperactivity (see Section 4.5).

On 2018 December 6, the HCN closely tracked the dust antisunward, while being comparatively enhanced in the projected sunward direction, and closely tracked H_2O (or was slightly more extended sunward; Figure 2). On 2018 December 14, similar to H_2O, HCN was broader than the dust; however, it was also more symmetric, i.e., its antisunward enhancement was not as pronounced as that of H_2O (Figure 2). On 2018 December 17, the HCN profile was narrower than H_2O in the NIRSPEC measurements (Bonev et al. 2021), indicating that HCN and H_2O likely have distinct outgassing sources. We did not have a sufficient signal-to-noise ratio on 2018 December 18 to extract an HCN profile for direct comparison with the contemporaneous NIRSPEC measurements; however, on 2018 December 19, the HCN spatial profile was similar to that for H_2O, and it was also enhanced antisunward. On 2018 December 21, all four HCN profiles (corresponding to the two mutually perpendicular PA sets) tracked H_2O relatively closely.

4.2.2. CH_3OH and C_2H_6

On 2018 December 6 (preperihelion) and 14 (postperihelion), CH_3OH and C_2H_6 showed similar spatial distributions (Figure 2). Specifically, both the gases were asymmetric, were broader in comparison to the comeasured dust profiles, and were enhanced sunward. While H_2O is clearly more antisunward-extended than HCN, it is less obvious that it is more antisunward-extended than C_2H_6 and CH_3OH; however, the C_2H_6 and CH_3OH spatial distributions are more sunward-enhanced than that of H_2O, and perhaps so is HCN. CH_3OH showed some interesting spatial features on 2018 December 16. Its profile, as obtained from all the available unblended lines, was clearly asymmetric, double-peaked, and sunward-enhanced, while being diminished in the antisunward direction. In contrast, H_2O, C_2H_6, and HCN as measured on the same night exhibited distinct (albeit symmetric) profiles (Figure 2, panels (E)–(G)). This behavior is consistent with the 46P Atacama Large Millimeter/submillimeter Array (ALMA)/Atacama Compact Array (ACA) studies of CH_3OH from nearly a week earlier, where similarly asymmetric line profiles favoring production in the sunward direction were observed (Roth et al. 2021b).

On 2018 December 18, the CH_3OH and OH^* (a proxy for the production rate and spatial distribution of H_2O; Bonev et al. 2006) spatial distributions were broader than the C_2H_6 profile, and both were enhanced antisunward (see Figure 3 in Roth et al. 2021a). Similar trends were observed in the contemporaneous NIRSPEC observation of 46P (Bonev et al. 2021), with the H_2O profile being broader than that for C_2H_6 and tracking the CH_3OH profile more closely, especially in the wings (∼50–100 km away from the peak gas intensity). On 2018 December 19, the two mutually perpendicular slit orientations, sampling distinct projections of the coma, resulted in some interesting features in both the dust as well as in the gases. The gas profiles corresponding to a PA of 113° (along the Sun–comet line) were broader than the dust profile, and slightly enhanced antisunward (Figure 3(A)). Conversely, the gas profiles corresponding to a PA of 23° were clearly asymmetric, broader than the dust, and also more enhanced antisunward (Figure 3(B)). This is in contrast to the results from 2018 December 6, 14, and 16, for which the enhancements in C_2H_6 and CH_3OH were sunward. Moreover, unlike the other dates, the C_2H_6 and CH_3OH profile shapes closely tracked the dust in both the slit positions. The slit position perpendicular to the Sun–comet line was more extremely asymmetric for both the volatiles and dust. This may suggest jet activity, where the dust and these species closely track one another, at least closer to the

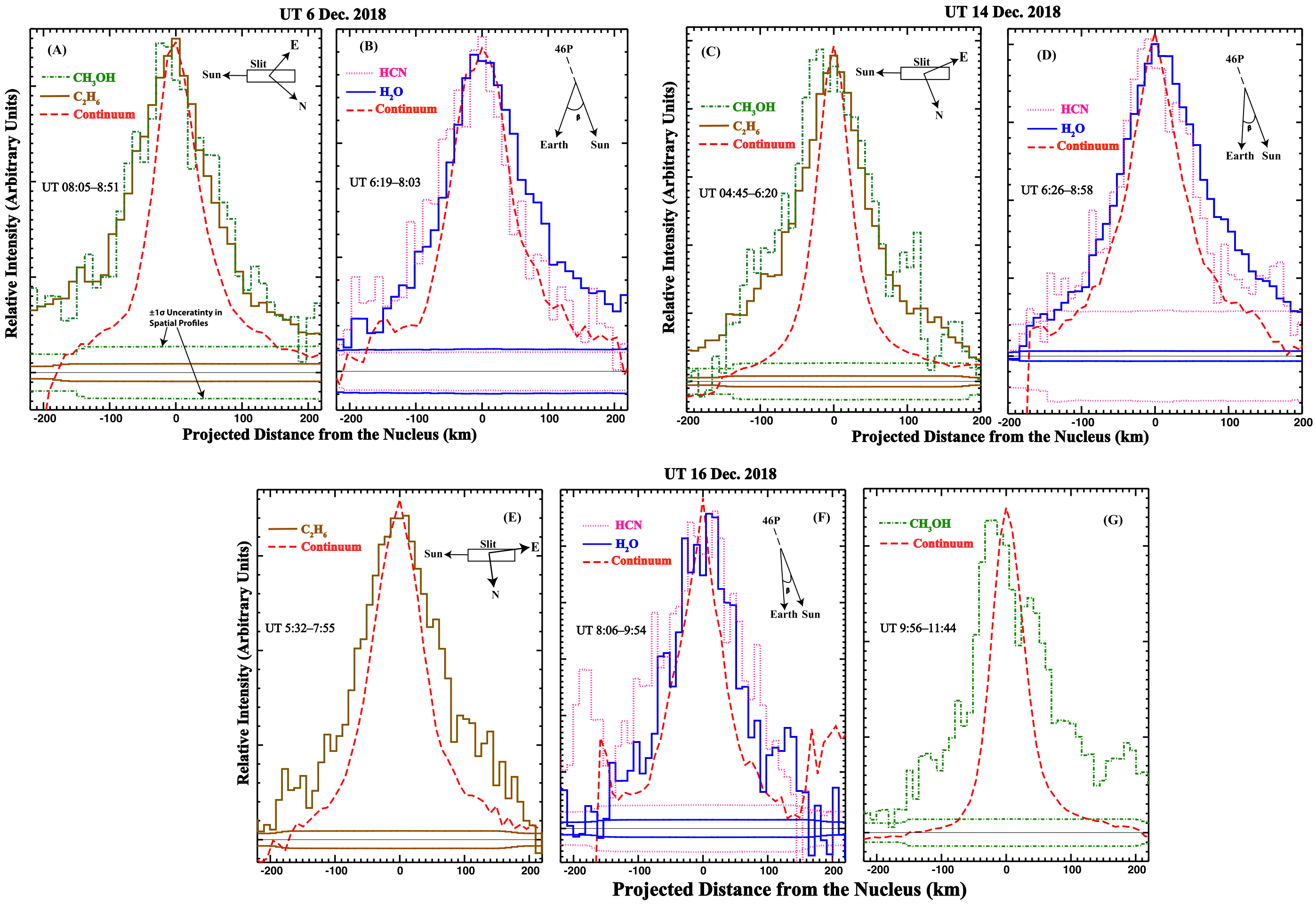

Figure 2. Emission spatial profiles of the primary volatiles and dust in 46P on UT 2018 December 6 ((A) and (B)), 14 ((C) and (D)), and 16 ((E), (F), and (G)). The profiles are color-coded, and comeasured profiles are overplotted on top of one another, after normalizing them to the profile with the highest intensity. The orientation of the slit on a given observing date along the Sun–comet line is indicated by the compass directions in panels (A), (C), and (E). The Sun–comet–Earth angle (phase angle, β) for each date is also shown in panels (B), (D), and (F). The UT intervals associated with the profiles are shown in each panel. The color-coded envelopes at the bottom of each panel represent the $\pm1\sigma$ uncertainties in the spatial profiles.

nucleus. The comet was observed for ∼1.5 hr with each of the two mutually perpendicular slit orientations (see Table 1). The total observing time corresponding to the two slit orientations was nearly one-third of the rotation period of 46P (Jehin et al. 2018). Thus, the rotation of the comet nucleus might have contributed to the observed differences in outgassing that were associated with the two slit orientations. We also note that on this date, there seemed to be very little difference in the shapes and widths of all the volatile profiles. On 2018 December 21, the relatively noisy CH_3OH profile was significantly broader when compared to that for C_2H_6, and both showed some antisunward enhancement. The results from our observations early in 2019 February (Saki 2021), suggesting similar dust, C_2H_6, and H_2O gas profiles, were similar to those for the 2018 December observations, possibly indicating a common source region on the nucleus. Combining these results, of CH_3OH being enhanced and broader on most of the observed dates, implies that, like H_2O, CH_3OH may also have had extended sources of outgassing in the coma. Ground-based measurements of the comet 103P/Hartley 2 (hereafter, 103P/H2) also indicated increased antisunward enhancements in the CH_3OH and H_2O outgassing, associated with sublimating icy grains in the coma (Dello Russo et al. 2011; Mumma et al. 2011; Bonev et al. 2013; Kawakita et al. 2013). In addition to being hyperactive comets, 46P and 103P/H2 have many other similarities (see Section 4.6.).

4.3. Production Rates and Mixing Ratios of Primary Volatiles

To interpret the mixing ratios of the primary volatiles and put them in context with those of other comets measured in the near-IR, we calculated weighted means of the measured mixing ratios on multiple dates. We also obtained the weighted means of these molecules in the following three epochs: (1) preperihelion (2018 December 6); (2) postperihelion, near the closest approach to Earth (2018 December 14 and 16; these dates were also near perihelion); and (3) postperihelion (2018 December 18–2019 February 5). These values, along with mean abundances in JFCs and over all comets, are shown in Table 3. The individual values used for calculating the weighted means are also shown in Figure 6.

We obtained the production rates of H_2O, C_2H_6, CH_3OH, and HCN (Figure 4) on nearly all the observed dates, while those for NH_3 and C_2H_2 (Figure 5) were obtained only on the 2018 December dates (except 2018 December 18). We aim to understand any asymmetry in the production rates about the perihelion, any possible variability in the production rates on timescales of days to weeks, and the effects of varying (albeit

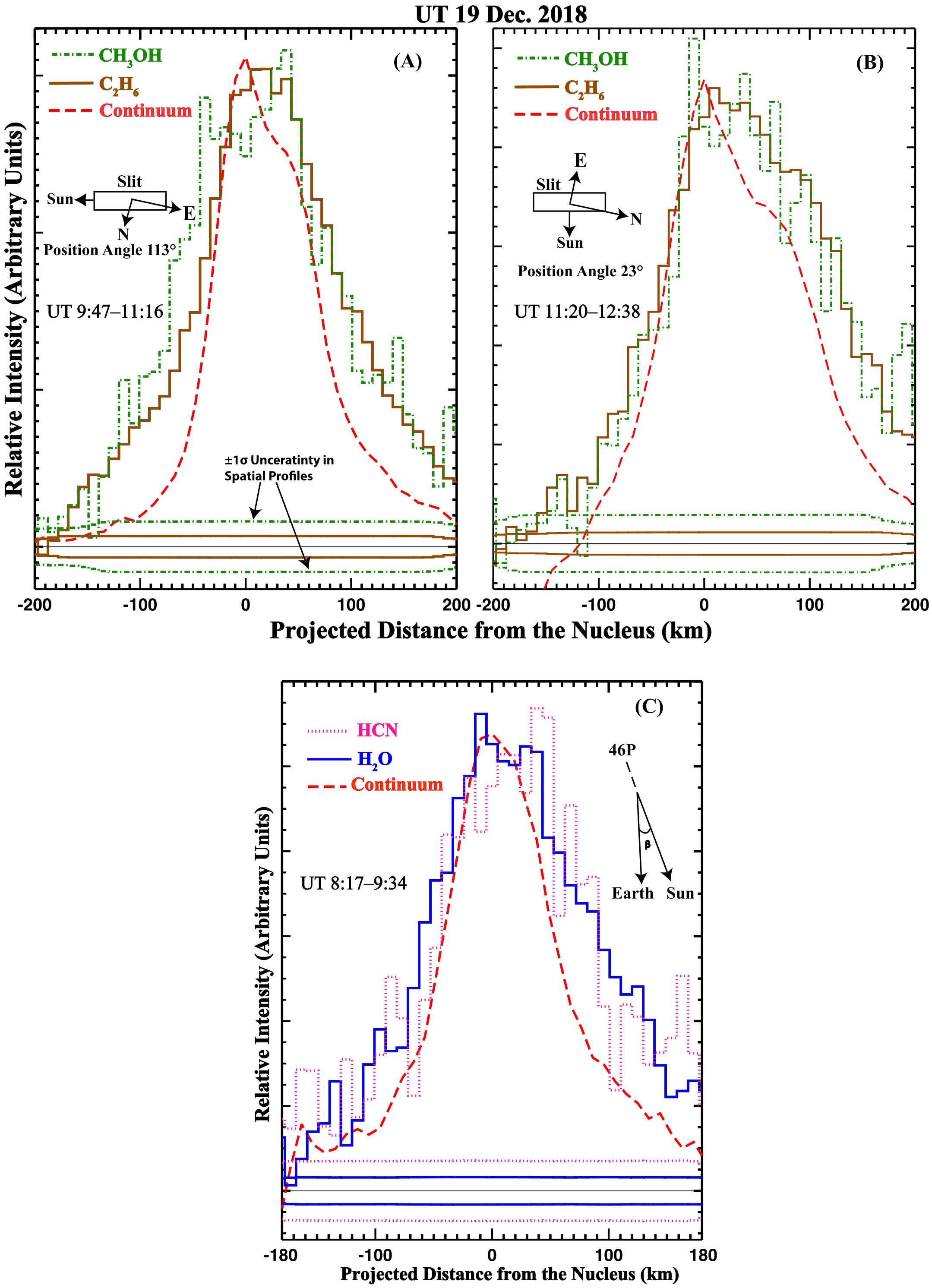

Figure 3. Spatial profiles of the primary volatiles in 46P on 2018 December 19. (A)–(B) Comeasured CH_3OH and C_2H_6, along with the comeasured dust profile, using PAs of 113° and 23°, respectively. (C) H_2O and HCN overplotted on one another, along with the comeasured dust, using a PA of 113°. The Sun–comet–Earth angle (phase angle, β) is also shown in (C). The UT intervals that are associated with the profiles are shown in each panel. The color-coded envelopes at the bottom of each panel represent the $\pm 1\sigma$ uncertainties in the spatial profiles.

not significantly) R_h on the production rates. Most importantly, we compare the trends in the H_2O production rates across the observed dates to those of the other molecules, as this is helpful in interpreting the abundances of the volatiles. Combined with the H_2O production rates, we will attempt to differentiate whether the variability in the volatile abundances is due to the variability in the trace species (e.g., CH_3OH and HCN) or whether it is due to the variation in the production of the reference molecule (H_2O or C_2H_6), or whether both factors are in fact contributing to the changes in the mixing ratios. For CH_3OH, C_2H_6, NH_3, HCN, C_2H_2, CO, CH_4, and H_2CO, we were able to obtain mixing ratios with respect to H_2O or stringent 3σ upper limits, as shown in Figure 6. The error bars represent the uncertainties in the mixing ratios, while the data

Table 3
Weighted Mean Mixing Ratios of the Primary Volatiles in 46P and the Mean Mixing Ratios in JFCs and in the Comet Population

Molecule[a]	Preperihelion[b]	Postperihelion—Closest Approach to Earth	Post Closest Approach to Earth and Postperihelion	Weighted Mean in 46P	Mean Value in JFCs[c]	[c] Mean Value in Comet Population
HCN	0.20 ± 0.01	0.22 ± 0.01	0.19 ± 0.01	0.20 ± 0.01	0.16 ± 0.02	0.20 ± 0.02
CH_3OH	3.55 ± 0.26	3.03 ± 0.17	2.76 ± 0.11	2.93 ± 0.09	2.24 ±0.40	2.27 ± 0.2
C_2H_6	1.10 ± 0.06	0.98 ± 0.05	0.82 ± 0.03	0.91 ± 0.03	0.40 ± 0.07	0.53 ± 0.06
C_2H_2	0.12 ± 0.01	0.09 ± 0.01	0.09 ± 0.01	0.10 ± 0.01	0.07 ± 0.02	0.12 ± 0.02
NH_3	1.1 ± 0.2	0.58 ± 0.06	0.58 ± 0.05	0.59 ± 0.04	0.50 ± 0.09	0.76 ± 0.16
H_2CO	⋯	⋯	0.09 ± 0.03	⋯	0.22 ± 0.07	0.27 ± 0.05
CO	⋯	⋯	<0.54	⋯	1.55 ± 0.36	4.20 ± 1.03
CH_4	⋯	⋯	<0.95	⋯	0.50 ± 0.11	0.72 ± 0.08

Notes.

[a] The 3σ upper limit values are not used in the calculations of the weighted means. For H_2CO, we only show the tentative detection obtained on 2018 December 19, whereas for CO and CH_4, we only show the most stringent 3σ upper limit.

[b] We only observed the comet on one preperihelion date (2018 December 6); these values are thus the same as those for 2018 December 6.

[c] Unweighted mean values in comets measured in the near-IR. The uncertainties in the means are the standard errors (i.e., the standard deviation from the mean divided by the square root of the number of measurements). These include the comets that are listed in Table 3 of Dello Russo et al. (2016) as well as the following comets, which were sampled more recently: C/2014 Q2 (Lovejoy; Dello Russo et al. 2022); C/2013 V5 (Oukaimeden; DiSanti et al. 2018); C/2012 K1 (PanSTARRS; Roth et al. 2017); C/2017 E4 (Lovejoy; Faggi et al. 2018); C/2018 Y1 (Iwamoto; DiSanti et al. 2021); C/2015 ER61 (PanSTARRS; Saki et al. 2021); 2P/Encke (Roth et al. 2018); 45P/Honda–Mrkos–Pajdušáková (DiSanti et al. 2017; Dello Russo et al. 2020); 21P/Giacobini–Zinner (Faggi et al. 2019; Roth et al. 2020); and 252P/Linear (Paganini et al. 2019). The mean values were calculated as follows. In the case of there being more than one measurement of a given molecule in a comet, we first calculated its weighted mean. Those weighted mean abundances were then used in the calculations of the unweighted means. In the case of there being only upper limit values for a molecule in a comet, we considered the most stringent upper limit X and used X/2 ± X/2 to calculate the unweighted mean.

points with downward arrows correspond to the 3σ upper limits of volatiles with no definitive detections. In Figures 4–6, the dates corresponding to the perihelion and the closest approach to Earth are marked by the vertical dashed black lines and dotted red lines, respectively. The heliocentric distances corresponding to each date are also shown at the tops of the figures.

Before discussing the production rates and mixing ratios of the primary volatiles, it is important to consider a caveat. The mixing ratios are defined as the production rates with respect to H_2O. The H_2O production rates were variable, especially in 2018 December, when the observations were closely spaced in time and the geocentric and heliocentric distances remained fairly constant, implying that these variations are not associated with changes in R_h. This observed variability in Q(H_2O) introduces a complexity into the interpretation and the comparison of the mixing ratios of volatiles from different dates—i.e., it becomes difficult to ascertain whether the changes in the abundance of a particular volatile are due to variability in its production rate, variability in water, or both. Also, if the Qs for any given molecule are increasing or decreasing proportionately to the corresponding Q(H_2O), the mixing ratios will not change, although the molecule is showing variation in its total gas production. The observed variability in Q(H_2O) has important implications for the mixing ratios of the primary volatiles, which will be discussed for each molecule. Figures 4 and 5 reveal some interesting insights into the production rates of the volatiles. In particular:

(a) All the volatiles showed different levels of variability across the observed dates. The maximum change in R_h was only about 0.25 au, which might have contributed to changes in the production rates as the comet moved toward or away from the Sun; however, changes in the production rates were noted even when R_h and Δ were essentially the same, indicating that other mechanisms dominated the variability.

(b) For nearly every molecule, the highest production rate was observed nearly 4–7 days postperihelion. For H_2O, CH_3OH, and C_2H_6, the highest Qs were obtained on the same date, 2018 December 18. We were not able to obtain Qs for HCN, C_2H_2, or NH_3 on this date, due to an insufficient signal-to-noise ratio. For HCN and C_2H_2, the highest Qs were observed on 2018 December 16. For NH_3, the highest Q was observed preperihelion (on 2018 December 6); however, given the higher uncertainty, this value is (marginally) consistent with its highest postperihelion Q (on 2018 December 19; Table 2).

(c) In general, the Qs for all molecules decreased on the first postperihelion date (2018 December 14), as compared to the only preperihelion date (2018 December 6), then increased to their highest values, with a drop following near 2018 December 21. CH_3OH also followed a similar trend, with the exception that its production rate did not show a drop on 2018 December 21.

(d) Our 2019 January 11–13 observations were separated from our 2018 December observations by only ~0.06 au in R_h. The Qs for C_2H_6, H_2O, and CH_3OH in 2019 January were lower overall than those from the 2018 December observations; however, for H_2O and HCN, our values on 2018 December 21 overlapped with those on 2019 January 11, being followed by an overall drop in Q(gas). For C_2H_6, all the 2019 January values were consistent with the 2018 December 21 value. The CH_3OH 2019 January values were consistent with one another.

As the most abundant and easily detectable volatile in comets, H_2O has been extensively used for calculating the mixing ratios of primary volatiles (Dello Russo et al. 2016 and references therein). Furthermore, in the near-IR, H_2O can be simultaneously measured with the primary volatiles discussed in this work (either directly or through its proxy OH^* emissions), thereby minimizing any setting-to-setting biases. That said, the importance of complementary compositional baselines, such as C_2H_6, has been demonstrated (for a comprehensive discussion of the merits of alternative baseline compositional studies and the case for C_2H_6, see Sections 4.12 and 5.4.2 of Bonev et al. 2021). Exploring the chemistry of comets using additional molecules as baselines can provide richer insights into their compositions, and can help with efforts to develop comet taxonomies based on mixing ratios

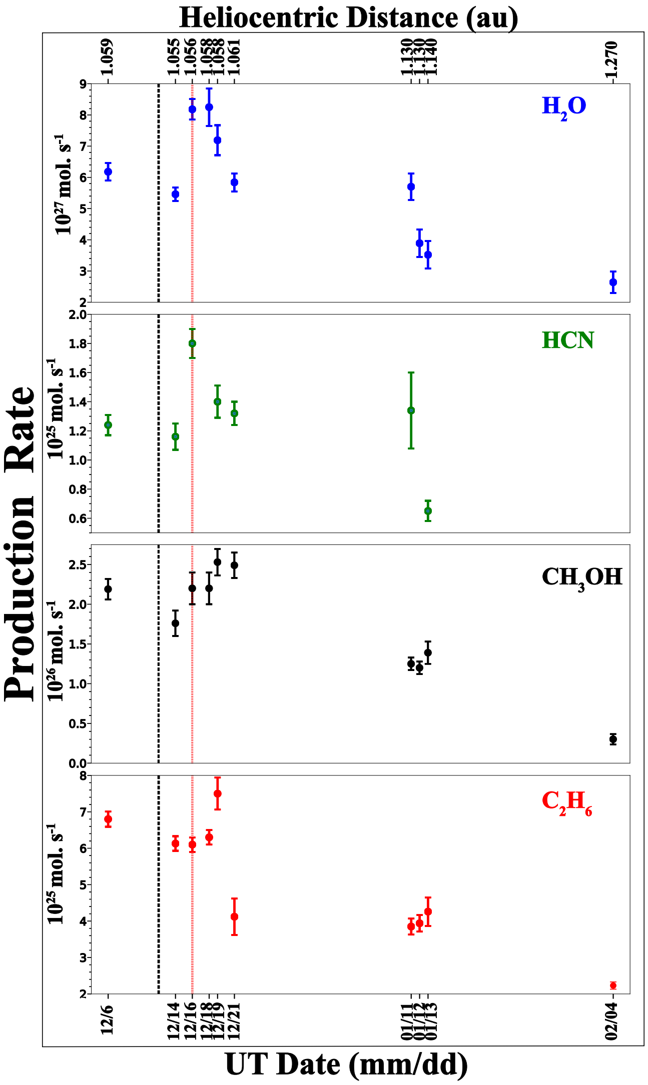

Figure 4. Production rates of H_2O (blue), HCN (green), CH_3OH (black), and C_2H_6 (red) in 46P during its 2018 apparition. The December dates correspond to 2018, whereas the January and February dates correspond to 2019. Volatiles with only upper limits are not shown. The uncertainties in the production rates are shown. The heliocentric distances are shown at the top of the figure. The vertical dashed black and dotted red lines represent the dates of the perihelion and the closest approach to Earth, respectively. The values corresponding to UT 2018 December 18 and 21 and 2019 January 11–13 and February 4 are taken from Roth et al. (2021a), Khan et al. (2021), McKay et al. (2021), and Saki (2021), respectively.

with respect to other molecules in addition to H_2O. We therefore calculated abundance ratios with respect to C_2H_6 as well as H_2O, which are shown in Table 2. In general, the missing ratios with respect to C_2H_6 were similar to those with respect to H_2O within the uncertainties; however, there were some notable exceptions. For example, on 2018 December 16, 18, and 21 and 2019 January 11, the mixing ratios with respect to C_2H_6 of most of the volatiles were higher in comparison to the corresponding values with respect to H_2O.

4.3.1. HCN

Hydrogen cyanide (HCN) is a precursor in the synthesis of amino acids, and thus an important organic for understanding the emergence of life. Bergman et al. (2022) used millimeter-wave observations and radiative transfer modeling to obtain HCN mixing ratios of (0.10 ± 0.01)% and (0.19 ± 0.02)% in 46P on 2018 December 21, using H_2O production rates from Combi et al. (2020) and Bonev et al. (2021), respectively. On 2018 December 21, we obtained a mixing ratio of ∼0.2% using comeasured Q(H_2O). The HCN production rate of $(1.57 \pm 0.12) \times 10^{25}$ mol s^{-1} obtained by Bergman et al. (2022) on 2018 December 20 was within the range of values that we obtained for 2018 December 21. Biver et al. (2021) obtained an average HCN mixing ratio of (0.11 ± 0.01)% from millimeter-wave observations of 46P spanning 2018 December ∼12–25. Wang et al. (2020) also obtained a similar average mixing ratio in 46P (0.09 ± 0.01)% on 2018 December 14 and 15. An important caveat to be considered while comparing the mixing ratios from near-IR and radio observations is that for reasons yet unknown, the near-IR HCN mixing ratios in comets are often higher by a factor of ∼2 than their corresponding values from radio observations (Bockelée-Morvan & Biver 2017). This discrepancy in the HCN mixing ratios measured at IR and radio wavelengths is evident here too.

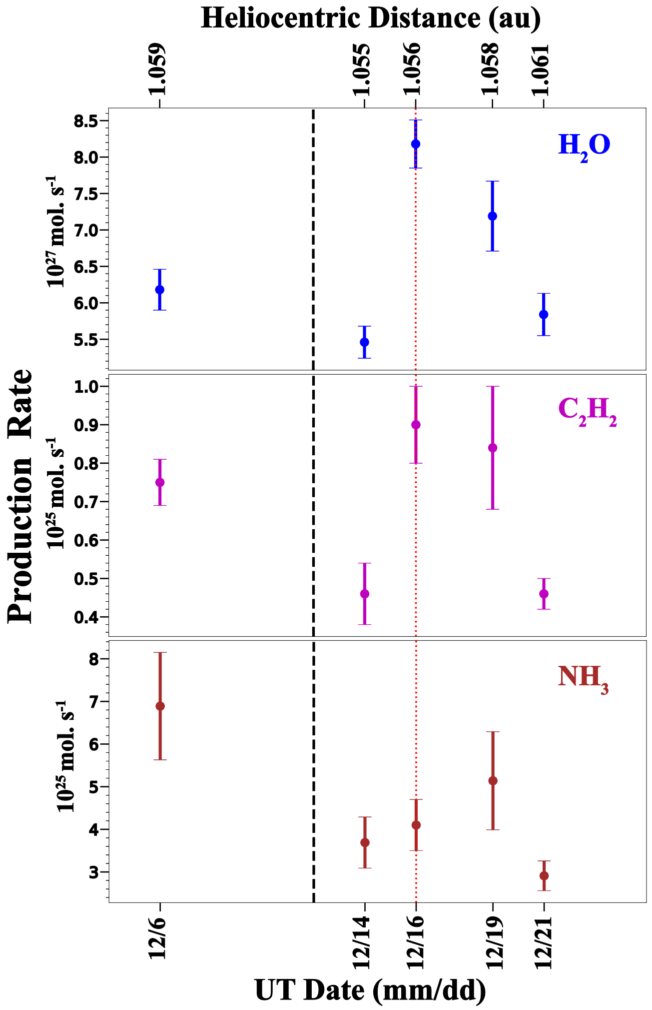

Figure 5. The production rates of H_2O (blue), C_2H_2 (purple), and NH_3 (brown) in 46P during 2018 December. The error bars show the uncertainties in the production rates. The heliocentric distances corresponding to all dates are shown at the top of the figure. The vertical dashed black line and the dotted red line represent the perihelion date and date of the closest approach to Earth, respectively. The values corresponding to UT 2018 December 21 are taken from Khan et al. (2021).

At optical wavelengths, the daughter species in comet comae are primarily sampled; however, it is not straightforward to

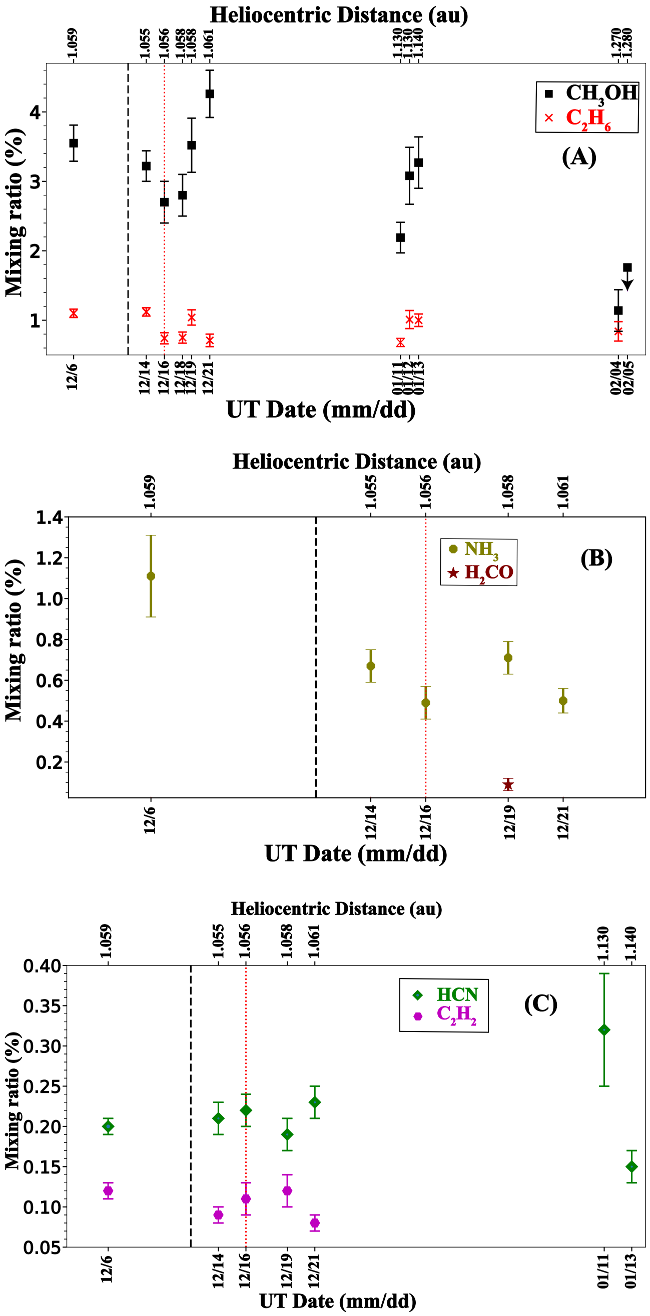

Figure 6. Mixing ratios with respect to H_2O of the primary volatiles CH_3OH and C_2H_6 (A), NH_3 and H_2CO (B), and HCN and C_2H_2 (C) in 46P during its 2018 apparition. The species are color-coded and the uncertainties in the mixing ratios are shown as the error bars. The 3σ upper limits of the mixing ratios are represented by the downward arrows. The heliocentric distances are shown at the top of each panel. The values corresponding to UT 2018 December 18 and 21 and 2019 January 11, 12, and 13 and February 4 and 5 are taken from Roth et al. (2021a), Khan et al. (2021), McKay et al. (2021), and Saki (2021), respectively. The vertical dashed black line represents the perihelion date, while the dotted red line shows the date of the closest approach to Earth.

connect these daughter species to their correct progenitors. At near-IR wavelengths, we sample primary/parent molecules; hence, connecting the two types of molecules is an important endeavor for tracking the lineage of the daughter species. For this reason, it is important to compare simultaneous or contemporaneous measurements from the two wavelength regimes. HCN is a significant parent source for CN, detected in many comets at optical wavelengths. Comparisons of the HCN and CN production in comets are important for understanding whether there are potentially other significant sources of CN in addition to HCN. E. Jehin (2020, private communication) reported a Q(CN) of $(1.27 \pm 0.032) \times 10^{25}$ mol s^{-1} on UT 2018 December 16 in 46P with narrowband photometry. D. Schleicher[16] deduced a similar Q(CN) (of 1.17×10^{25} mol s^{-1}) on the same date. A comparison with our Q(HCN) leads to a Q(CN)/Q(HCN) of ∼0.65–0.70, suggesting that HCN is likely the dominant source of CN in 46P.

We have consistently obtained HCN mixing ratios of ∼0.2% in 46P (Table 2 and Figure 4). HCN most closely followed the trend in Q(H_2O) among the trace species. On 2018 December 21, we obtained four data sets (corresponding to two different PAs) and observed that the trends in the H_2O and HCN production rates on timescales of minutes were extremely similar (Figure 4 in Khan et al. 2021). Our weighted average HCN mixing ratio of ∼0.2% is consistent with the Rosetta value from 67P/CG (Biver & Bockelée-Morvan 2019; Rubin et al. 2019; Läuter et al. 2020), and is within the range of values for comets (0.08%–0.25%; Biver et al. 2021). On 2019 January 11, we obtained a Q(HCN) value of (0.32 ± 0.07)%, which is slightly higher compared to the 2018 December dates, if the uncertainties are taken into account. On 2019 January 13, however, we obtained a Q(HCN) value that was nearly half that of two days prior. Q(H_2O) also decreased over these two days, implying that the decrease in Q(HCN) was more pronounced than that of H_2O on this date. The general consistency in the mixing ratios with respect to H_2O during the apparition of 46P also suggests that the HCN and H_2O activity might be positively correlated in 46P.

4.3.2. *CH_3OH*

Methanol is among the more abundant species in comets, ranging from 0.4%–6.2% (Dello Russo et al. 2016; Bockelée-Morvan & Biver 2017). It is routinely detected in comets at near-IR wavelengths, owing to its many strong lines. Biver et al. (2021) obtained nearly two dozen measurements of the CH_3OH production rates between 2018 December 11.89 and 25.83, using millimeter-wave observations. They obtained Q(CH_3OH) values spanning $\sim 2\text{–}3.5 \times 10^{25}$ mol s^{-1} (Table 5 in Biver et al. 2021). On nearby and some overlapping dates between 2018 December 6 and 21, we obtained production rates that were generally within this range, and our individual Qs agreed within uncertainties with the average found by them. Coulson et al. (2020) reported a higher production rate of $(3.5 \pm 0.2) \times 10^{26}$ mol s^{-1} using JCMT on 2018 December 16 and 18.

The CH_3OH production rates and mixing ratios exhibited significant variability in 46P, with the values of the mixing ratios ranging from 1.14% to 4.26%. The weighted mean of ∼3% implies that 46P is on average enriched in CH_3OH when compared to the mean values among both JFCs and the comet population. Similarly enriched values of CH_3OH have been observed in other short-period comets, such as 2P/Encke (3.48%; Radeva et al. 2013), 45P/Honda–Mrkos–Pajdušáková (hereafter, 45P/HMP; 3.59% and 4.51%; DiSanti et al. 2017 and Dello Russo et al. 2020, respectively), and 252P/LINEAR (4.87%; Paganini et al. 2019).

---

[16] https://wirtanen.astro.umd.edu/46P/46P_status.shtml

Biver et al. (2021) reported a mixing ratio of 3.38% ± 0.03% on nearby dates, and Coulson et al. (2020) reported a slightly higher mixing ratio of ~5%. Using millimeter-wave observations from 2018 December 22–28, Bergman et al. (2022) derived a mixing ratio of 1.6%, lower than our 2018 December values. A similar variability was found by Roth et al. (2021b), who reported the CH_3OH production rates from ACA/ALMA measurements of 46P on 2018 December 8–9. Their overall production rates were consistent with ours. They also reported variability on timescales of minutes, as well as anisotropic outgassing behavior consistent with the rotational period of 46P, most probably associated with differences in the nucleus illumination due to rotation. We obtained the highest CH_3OH mixing ratio (4.26%) on 2018 December 21. On this date, the Q(H_2O) was lower as compared to that of the previously observed date (2018 December 19), while Q(CH_3OH) remained nearly constant. Using the value of Q(H_2O) from 2018 December 19, we obtain a mixing ratio of ~3.5% on 2018 December 21, which is consistent with the mixing ratio on 2018 December 19, implying that the variability in the mixing ratio between the two dates is solely due to a decrease in Q(H_2O).

The 2019 January and February observing dates were separated by ~three weeks, and during this time the comet only moved ~0.15 au from the Sun. This change in R_h might have contributed to the decrease in Q(CH_3OH), as shown in Figure 4. Between 2019 January 13 and February 4, the abundance of CH_3OH decreased by ~65%, while Q(CH_3OH) and Q(H_2O) decreased by ~78% and 38%, respectively, indicating that the decrease in the mixing ratio was due to a decrease in Q(CH_3OH).

In general, CH_3OH is enriched in 46P, while H_2CO is depleted, resulting in one of the highest alcohol-to-aldehyde ratios measured in comets (Dello Russo et al. 2016). Alcohol-to-aldehyde ratios in comets—e.g., via measurements of CH_3OH and H_2CO—are important for understanding the relationship between the two molecules. In the interstellar medium, the former is thought to be predominantly formed through the latter (however, experimental formations of CH_3OH, via $CH_4 + OH \rightarrow CH_3 + H_2O$ and $CH_3 + OH \rightarrow CH_3OH$, have also been shown; Qasim et al. 2018).

4.3.3. C_2H_6

C_2H_6 is routinely measured in comets, owing to its strong emission lines and relatively high abundance. We detected C_2H_6 on all the observed dates, except UT 2019 February 5. Figure 6(A) shows that the mixing ratio of C_2H_6 exhibits variability, and that the mixing ratios are clearly divided into two distinct groups, with most of the values either around 0.7% or 1.1%. Figure 4 shows that on 2018 December 16 and 18, the H_2O production rates clearly display enhancement as compared to the that of the previously observed date, while the Q(C_2H_6) values are clearly consistent over the three dates. This results in a lower mixing ratio between 2018 December 14 and the next two observing dates, implying that this particular variability in the mixing ratio is solely dictated by the changes in Q(H_2O). There is a decrease of ~45% in Q(C_2H_6) between 2018 December 19 and 21, when the R_h and Δ remained practically the same. In contrast, Q(H_2O) changed by only 18% between the two dates, implying that the change in the mixing ratio of Q(C_2H_6) between the two dates (Figure 6(A)) is due to the variability in Q(C_2H_6). The weighted mean of the C_2H_6 abundances across the observed dates is significantly higher than the mean values among both JFCs and the overall comet population (Table 3), implying that C_2H_6 is enriched in 46P. This is interesting, because C_2H_6 has a lower sublimation temperature (only higher than CO and CH_4 among the molecules discussed in this work), and its abundance is on average lower in JFCs as compared to OCCs (Dello Russo et al. 2016).

4.3.4. C_2H_2

C_2H_2 is a symmetric hydrocarbon, which is important for constraining hydrocarbon chemistry in comets. Its emissions are moderately strong, although some of the strong lines are blended with lines from other molecules, making it challenging to quantify. Spatial profiles and $T_{\rm rot}$ for C_2H_2 are thus rarely obtained in comets, including in this study. Despite these difficulties, we were able to clearly detect C_2H_2 in 46P on multiple dates (all dates in 2018 December, except 2018 December 18). In 2019 January and February, the comet was too faint to detect C_2H_2. We assumed that the well-constrained $T_{\rm rot}$ and GF from the comeasured H_2O and/or HCN were the same for C_2H_2 to obtain the production rates and abundances. We noticed an appreciable variation in the production rates between the dates spanning 2018 December 6–21 (Figure 5), but only small variations in the mixing ratios between those dates, indicating that the Qs of C_2H_2 and H_2O were changing proportionately, suggesting that they are perhaps associated in the nucleus. In the interstellar medium, C_2H_2 is thought to form in the carbon grains that are formed in the ejecta of C-rich stars, while H_2O is formed on top of the grains (Contreras & Salama 2013). C_2H_2 can also potentially be formed in the H_2O-rich ice phase, via C and H atom accretion (D. Qasim, private communication). The C_2H_2 mixing ratios in 46P ranged between ~0.08% and 0.12%. The weighted mean value of the C_2H_2 mixing ratio of 0.10 ± 0.01 in 46P agrees with the mean abundances in JFCs and the comet population (see Table 3). The C_2 radical observed in many comets at optical wavelengths is a daughter molecule of C_2H_2. A comparison of C_2H_2 and C_2 is therefore important for understanding the latters's progenitors. On 2018 December 9, E. Jehin (private communication) reported Q(C_2) of $(1.90 \pm 0.025) \times 10^{25}$ mol s^{-1} and Q(OH) of $(5.22 \pm 0.120) \times 10^{27}$ mol s^{-1}, giving Q(C_2)/Q(OH) of 0.36%, nearly three times greater than our Q(C_2H_2)/Q(H_2O) obtained nearly three days earlier. This implies that C_2H_2 might not be the primary precursor of C_2.

4.3.5. NH_3

The detection of ammonia in comets is challenging, owing to the few weak unblended lines that are available at near-IR wavelengths. We detected NH_3 on multiple dates in 2018 December by combining lines from multiple orders. Because the comet was farther from the Sun, we did not detect NH_3 on any of the 2019 January and February dates. The NH_3 mixing ratios ranged between 1.11% and 0.49% (Table 2). Q(H_2O) and Q(NH_3) showed a decrease on the first postperihelion date, when compared to the preperihelion date; however, the decrease in Q(NH_3) was more drastic, as indicated by the decrease in mixing ratios between the two dates. Between 2018 December 14 and 16, the Q(NH_3) are consistent with one another within uncertainty; however, the mixing ratios differ slightly, owing to the large (~50%) increase in Q(H_2O). We obtained a weighted mean value of 0.59 ± 0.04, which is consistent with the mean values among JFCs and the comet population, within uncertainty.

4.3.6. H_2CO

H_2CO lines in the near-IR are generally weaker in comets, and many are also blended with lines from other stronger species (such as CH_3OH), making their detection challenging. The H_2CO abundances range from 0.04% to 1.3% in comets (Dello Russo et al. 2016; Bockelée-Morvan & Biver 2017), and despite its low abundance, H_2CO has been detected in more than 20 comets in the near-IR (see Tables 3–4 in Dello Russo et al. 2016). We were only able to obtain a tentative detection of H_2CO on 2018 December 19, by combining lines in the orders 144 and 145 from the two mutually perpendicular slit orientations in the Lp1 setting. On some other dates, we obtained 3σ upper limits that were consistent with the tentative detection on 2018 December 19 (see Table 2). H_2CO was depleted in 46P, as compared to the mean values for the comet population and JFCs.

When interpreting our H_2CO upper limits, it is important to consider the iSHELL field of view, coupled with the small geocentric distance of 46P during our measurements. H_2CO is more easily measured through its rotational transitions at millimeter/submillimeter wavelengths, where extensive work has demonstrated significant coma production of H_2CO (e.g., Biver et al. 1999; Bockelée-Morvan et al. 2000; Cordiner et al. 2014). Biver et al. (2021) calculated $H_2CO/H_2O = (0.38 \pm 0.02)\%$ in 46P, using the IRAM 30 m radio telescope, consistent with the average values for comets (Bockelée-Morvan & Biver 2017). When considering the $\sim 11''$ IRAM beam size compared to our $2''.5$ nucleus-centered extracts, it is possible that the IRAM measurements were more sensitive to H_2CO production in the coma at greater nucleocentric distances, whereas our measurements placed stringent upper limits on H_2CO production at or near the nucleus.

4.3.7. CO and CH_4

CO and CH_4 are the most volatile species that are detected in comets at IR wavelengths, and they are on average depleted in JFCs, as compared to OCCs (Dello Russo et al. 2016; DiSanti et al. 2017). To shift their emission lines away from their strong terrestrial counterparts, a sufficiently high Δ-dot ($\sim$13 km s^{-1} or more) is required. This has resulted in the underrepresentation of the hypervolatile measurements in JFCs, which are generally fainter than OCCs and have lower Δ-dot values close to Earth, when they are generally brightest and most favorable for spectroscopic measurements. Owing to these limitations, we were only able to obtain upper limits for CO and CH_4 in 46P (see Table 2), when the Δ-dot was sufficiently high. Our most stringent 3σ upper limits of $\sim$0.5% and $\sim$1% for CO and CH_4, respectively, indicate that CO is likely depleted in 46P, as compared to JFCs and the comet populations, while CH_4 is likely to be either typical or depleted.

4.3.8. HC_3N

The detection of HC_3N (cyanoacetylene) in comets at near-IR wavelengths is challenging, because of its low abundance and the large number of emissions in the same spectral region as more abundant species (see Section 4.12 of Khan et al. 2021 for details). In 46P, we obtained a sensitive 3σ upper limit of 0.007% for HC_3N on 2018 December 21 (Khan et al. 2021), by combining lines from the four L-Custom data sets. Biver et al. (2021) obtained a more stringent upper limit (0.003%) using the IRAM 30 m radio telescope. Saki et al. (2021) obtained 3σ upper limits on the HC_3N abundances on three dates in comet ER61, ranging from 0.01% to 0.04%. An upper limit of 0.0043% was recently reported for comet C/2014 Q2 Lovejoy (Dello Russo et al. 2022), indicating that HC_3N is less abundant in comets. We note that HC_3N has to date been detected in multiple comets at millimeter/submillimeter wavelengths (Bockelée-Morvan & Biver 2017), but only 3σ upper limits have been calculated for a few comets at near-IR wavelengths.

4.4. Variability in 46P and Range of Abundances in Comets

To put the observed variability into context, we compare the abundances in 46P with the values found in comets observed in the near-IR, as shown in Figure 7. For CH_4 and CO, we show only the most stringent 3σ upper limits, represented by the downward arrows, while for H_2CO we show the most stringent upper limit and the tentative detection on 2018 December 19. We compare these abundances with the values that have been measured to date in comets from ground-based near-IR observations (green triangles), the weighted mean abundances in 46P (blue circles), and the mean abundances in the comet population (red diamonds).

Variability in the mixing ratios has been noted in many comets. For example, in 67P/CG, the Rosetta mission found that the mixing ratios of CO and CO_2 in the coma varied due to seasonal effects on the nucleus (Hässig et al. 2015). Similarly, variation in the volatile mixing ratios has been found on smaller timescales, with some volatiles (such as CH_4) showing diurnal variations, which differed from those for other volatiles, such as CO and C_2H_6 (Luspay-Kuti et al. 2015; Bockelée-Morvan et al. 2016; Fink et al. 2016). Comet 2P/Encke also showed significant variation in the mixing ratios of some of its molecules between its 2003 and 2017 apparitions (Radeva et al. 2013; Roth et al. 2018). That said, there have been other comets in which there was either no variability in the mixing ratios (e.g., 103P/H2; Mumma et al. 2011) or it was not significant when compared to the range of values found in comets (e.g., 21P/Giacobini–Zinner; Roth et al. 2020). Figure 7 shows that although the primary volatiles showed variation in the mixing ratios, the spread in values remained strictly well within the range of values found in comets. The most pronounced variation in 46P was noted in CH_3OH.

4.5. H_2O Production Rates in 46P and Insights into Its Hyperactivity

With an effective radius of $\sim$0.6–0.7 km (Lamy et al. 1998; Boehnhardt et al. 2002), 46P is among the smallest known periodic comets (Snodgrass et al. 2011); it is also among the few known hyperactive comets. By definition, a hyperactive comet exhibits higher water production rates than expected from its nucleus size and standard water vaporization models (Cowan & A'Hearn 1979). In hyperactive comets, the water production rate requires a sublimating surface area comparable to the total nucleus area, whereas most comets have an active fraction (the surface area required to sustain the water production rate divided by the total surface area) of a few to 30% (A'Hearn et al. 1995; Protopapa et al. 2021 and references

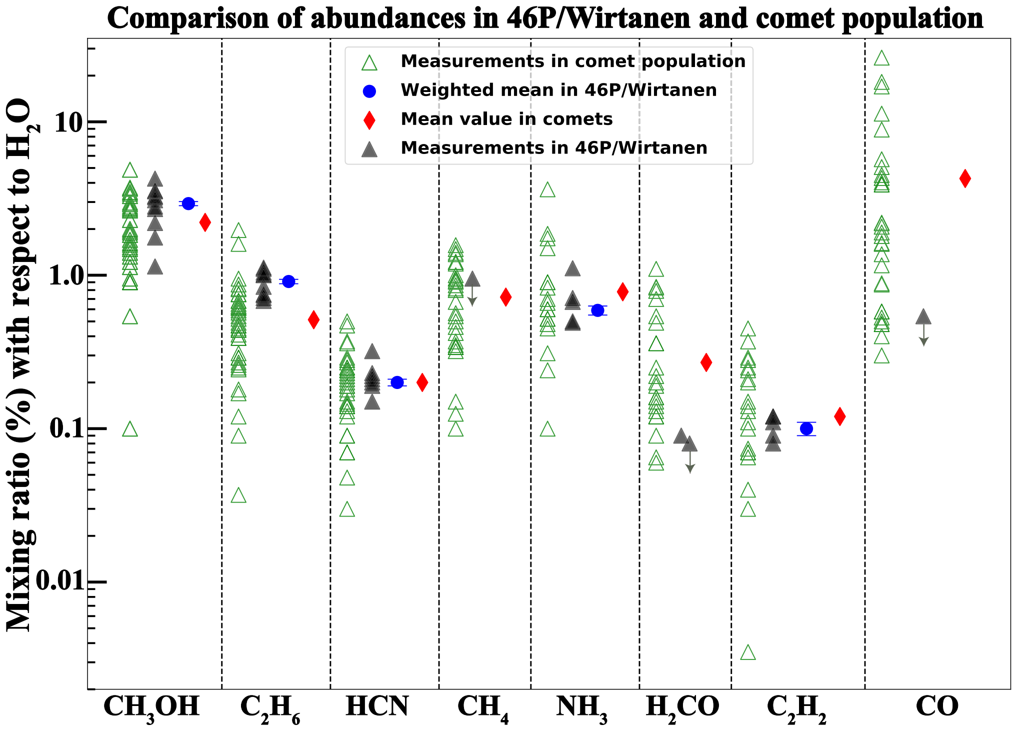

Figure 7. Mixing ratios of the primary volatiles in 46P (black triangles) compared with the values in the comet population (open green triangles). The weighted means of the mixing ratios in 46P are represented by the blue circles, whereas the red diamonds represent the mean mixing ratios in the comet population sampled in the near-IR. The most significant 3σ upper limits in 46P are represented by the downward arrows. For the comets that are shown in this figure, see Table 3 in Dello Russo et al. (2016) and the notes to Table 3 in this work.

therein). Comet 46P has been identified as a hyperactive comet (Lamy et al. 1998; Groussin & Lamy 2003; Lis et al. 2019), with an active fraction between 60% and 120% at perihelion, during the 1997 and 2002 apparitions. Protopapa et al. (2021) estimated an active fraction of ∼60% for 46P near perihelion in 2018, using the sublimation model of Cowan & A'Hearn (1979). Our 2019 January 11–13 measurements imply an active fraction of ∼30%–40% (see Sections 3.3 and 4.2 of McKay et al. 2021). Kobayashi & Kawakita (2010) combined measurements from multiple apparitions, and found that 46P's H_2O production was repeatable from one apparition to the next, with little evidence for secular variation; however, power-law fittings of the Solar and Heliospheric Observatory (SOHO)/SWAN measurements (which were obtained relative to photodissociation products) by Combi et al. (2019) suggest that the H_2O production rates decreased significantly between the 1997/2002 and 2008/2018 apparitions, along with a large steepening of Q(H_2O) with R_h. These changes are similar to those observed for comet 103P/H2 between its 1997 and 2011 apparitions (Combi et al. 2011).

The H_2O production rates exhibited variability in 46P during its 2018 apparition. For example, between 2018 December 14 and 21, the changes in R_h and Δ were minimal (Table 1), but we observed production rates on 2018 December 16, 18, and 19 (Figure 4) that were higher than the 2018 December 14 and 21 values by ∼30%. The highest production rate during the entire apparition was recorded on 2018 December 18 (nearly six days after perihelion). Bonev et al. (2021) also reported a higher water production rate on 2018 December 18 (consistent with our numbers, within uncertainty), using the then newly upgraded NIRSPEC spectrograph (Martin et al. 2018). The higher water production rates on 2018 December 16, 18, and 19, together with 46P's hyperactivity, could be explained by the presence of extended sources of H_2O outgassing (e.g., icy grains) in the inner coma of the comet. Bonev et al. (2021) confirmed the presence of possible extended sources in the coma in two ways: (a) the H_2O spatial profile was systematically broader, as compared to other species (HCN, C_2H_2, and C_2H_6), which is an indication of extended release in the coma; and (b) a nearly constant rotational temperature with (projected) distance from the nucleus was explained on the basis of extended icy grains or chunks in the coma. In the case of the H_2O production solely via direct nucleus sublimation, collisions equilibrate the rotational temperature to the kinetic temperature of the gas (Combi et al. 2004) in the inner coma; however, the heat generated by the vaporization of water from icy grains works against the near-adiabatic cooling of the coma, keeping the rotational temperature nearly constant (for details, see Sections 4.1 and 4.2 of Bonev et al. 2021). While other possible mechanisms for explaining the T_{rot} versus distance-from-the-nucleus profiles for H_2O are discussed (e.g., dissociation fragments and electron collisions), a significant icy grain source in the coma is the most plausible explanation. Moreover, the EPOXI flyby mission to 46P's "twin" comet, 103P/H2, established in situ confirmation of water–ice grains being ejected into the coma, which effectively mimicked additional active surface area, to explain its observed hyperactivity (A'Hearn et al. 2011; Kelley et al. 2013; Protopapa et al. 2014). The ejection of H_2O ice grains into the coma was attributed to the more volatile CO/CO_2-dominated jets that were clearly identified by the EPOXI mission. Given the evidence discussed, a similar mechanism may also be responsible for 46P's hyperactivity. Protopapa et al. (2021) ruled out the presence of water–ice grains in the coma of 46P, based on the absence of water–ice absorption bands at 1.5, 2.0, and 3.0 μm. They argued, however, that the hyperactivity of

Table 4
Comparison of the Mixing Ratios (with Respect to H_2O; in %) of the Primary Volatiles in 46P with Other Hyperactive JFCs

Comet	HCN	C_2H_2	NH_3	CH_3OH	C_2H_6	CO	CH_4	H_2CO
46P[a]	0.20 ± 0.01	0.10 ± 0.01	0.59 ± 0.04	2.93 ± 0.09	0.91 ± 0.03	<0.54	<0.97	0.09 ± 0.03
46P[b]	0.20 ± 0.01	0.074 ± 0.013	$0.66^{+0.11}_{-0.29}$	3.03 ± 0.23	0.76 ± 0.06	…	…	<0.064
45P/HMP[c]	0.15 ± 0.02	0.07 ± 0.02	0.16-1.5	4.51 ± 0.54	0.81 ± 0.07	<3.7	1.0 ± 0.2	0.14 ± 0.03
45P/HMP[d]	0.049 ± 0.012	0.076 ± 0.026	0.64 ± 0.24	3.59 ± 0.3	0.52 ± 0.04	0.6 ± 0.04	0.79 ± 0.06	0.36 ± 0.04
103P/H2[e]	0.24 ± 0.01	0.10 ± 0.01	0.66 ± 0.06	1.95 ± 0.07	0.75 ± 0.02	0.3 ± 0.15	<0.47	0.13 ± 0.02

Notes.

[a] This work. For CO and CH_4, only the most stringent 3σ upper limits are listed. For H_2CO, only the tentative detection value on 2018 December 19 is shown. All other abundances are the weighted means from measurements on multiple dates.

[b] Bonev et al. (2021).

[c] Dello Russo et al. (2020).

[d] DiSanti et al. (2017).

[e] Kawakita et al. (2013); Mumma et al. (2011); Dello Russo et al. (2011); and Weaver et al. (2011). See Table 1 of Dello Russo et al. (2016) for details.

46P, combined with the absence of water–ice absorption features in their spectra, could be explained either by icy grains of the order of 1 μm in size, with a small amount of dust, or by large chunks containing significant amounts of water. They ruled out the possibility of pure ices as the extended sources of outgassing. The degree of contribution from icy grains to water production may vary, and it also depends on the field of view of the instrument used. Bonev et al. (2021) estimated that the extended sources might have contributed at least ∼35% to the total production rate. Combi et al. (2019) also reported higher H_2O production rates on 2019 January 11, 12, and 13 from SOHO/SWAN, as compared to our contemporaneous iSHELL observations (McKay et al. 2021) on the same dates. The extra ∼40% excess production of H_2O might be due to icy grains that are more extended in the coma and could only be detected with a larger field of view, such as that of SOHO/SWAN.

Using narrowband filter photometry, Knight et al. (2021) obtained a peak value of $Q(H_2O) = 8 \times 10^{27}$ mol s^{-1} on 2018 December 3, using the empirical conversion from a Haser OH production rate to the equivalent vectorial H_2O production rate. They obtained 7.2×10^{27} mol s^{-1} on 2018 December 16 (nearly four days after perihelion), which is comparable to our $Q(H_2O)$ of $\sim 8 \times 10^{27}$ on the same date. Moulane et al. (2019) obtained $(7.20 \pm 0.24) \times 10^{27}$ at perihelion, slightly higher than what we obtained ∼2 days later, on 2018 December 14.

4.6. 46P and Other Known Hyperactive Comets

In addition to 46P, the JFCs 41P/Tuttle–Giacobini–Kresák (Combi et al. 2020), 45P/HMP (Lamy et al. 1999), and 103P/H2 (Groussin et al. 2004), as well as the OCC C/1996 B2 Hyakutake (Lisse et al. 1999), are among the members of the small group of known hyperactive comets. The hyperactivity of a comet might have crucial implications for water on Earth, as there is evidence that the D/H ratio in comets decreases and tends to approach terrestrial values with increasing hyperactivity (Lis et al. 2019). The hyperactive JFCs 103P/H2, 45P/HMP, and 46P have D/H ratios similar to the terrestrial value (VSMOW; Hartogh et al. 2011; Lis et al. 2013, 2019). There are, however, indications of diversity in the D/H ratios among JFCs and OCCs. For example, the Rosetta target comet 67P/CG had a D/H ratio three times that of VSMOW (Altwegg et al. 2015), while OCC C/2014 Q2 had a D/H ratio compatible with VSMOW (Biver et al. 2016).

In addition to hyperactivity, 46P and 103P/H2 have other similar features, such as smaller sizes and similar secular changes in water production rates over the past ∼20 yr. 45P/HMP, however, has not experienced any such secular change over the past two decades (Combi et al. 2020). 46P and 103P/H2 have similar compositional profiles as well. The CO_2 mixing ratio with respect to H_2O as observed by the EPOXI mission ranged between 10% and 20% (A'Hearn et al. 2011), which encompassed the range of values inferred for 46P from [O I] observations (McKay et al. 2021). The CO_2 abundance for 45P/HMP is unknown as yet. Table 4 shows the weighted mean abundances in 46P (this work) in comparison with its composition on 2018 December 17 and 18, as measured with NIRSPEC (Bonev et al. 2021), and the compositions of comets 45P/HMP and 103P/H2. 46P, 45P/HMP, and 103P/H2 have similar compositions. When compared to the mean value for JFCs, these comets have higher-than-average CH_3OH and C_2H_6, typical HCN, NH_3, and C_2H_2, and most likely depleted H_2CO, and CO. We note that there are exceptions in some measurements, and that the upper limits for CH_4 in 46P and 103P/H2 do not allow us to conclude whether CH_4 is typical, depleted, or enriched; however, the two values in 45P/HMP point toward enrichment. The overall similarities in the group of hyperactive JFCs raise some important questions, such as. (a) Do all (or most) hyperactive comets have terrestrial D/H, and if yes, what is their potential role in delivering water to Earth? (b) Are there other hyperactive comets with similar compositions that could potentially be categorized into a subgroup of comets? (c) Do these JFCs point toward a region of similar composition in the protoplanetary disk? (d) Are hyperactive JFCs and OCCs compositionally similar or distinct?

These questions are crucial to our understanding of the early solar system, and they could be better understood with more observations of hyperactive JFCs and OCCs in all aspects, including their sizes, activity drivers and active fractions, compositions, and isotopic ratios.

5. Summary and Conclusions

1. We obtained high-resolution IR spectroscopic data for 46P during its historic 2018 apparition on 11 dates spanning ∼two months, from 2018 December to 2019 February, using the iSHELL spectrograph at the NASA IRTF.
2. We obtained emission spectra, rotational temperatures, production rates, and mixing ratios (or sensitive upper limits) with respect to H_2O and C_2H_6 of a large suit of

primary volatiles, including H_2O, HCN, C_2H_2, NH_3, H_2CO, C_2H_6, CH_3OH, CH_4, CO, and HC_3N.

3. The H_2O production rates exhibited variability across the observed dates.
4. The primary volatile mixing ratios with respect to H_2O also showed variability, either due to changes in the H_2O production rate or changes in the production rates of the volatiles.
5. We obtained spatial profiles to understand the spatial distribution of and associations among the primary volatiles in the coma. In general, H_2O showed broader spatial profiles, consistent with extended sources of outgassing in the comet's coma. We also discussed the hyperactivity of 46P, which is most likely due to the extended secondary sources of outgassing, such as icy grains/chunks in the coma, similar to the EPOXI mission target 103P/H2.
6. We noticed similarities in the compositions of 46P and the other hyperactive comets 45P/HMP and 103P/H2.
7. We calculated weighted means of the mixing ratios of primary volatiles from multiple measurements, and compared them with the mean values among JFCs and the comet population measured in the near-IR wavelength. We also compared our results with those obtained from other wavelength ranges, such as optical and radio.

Data for this study were obtained at the NASA Infrared Telescope Facility, operated by the University of Hawai'i, under contract NNH14CK55B with NASA. We are extremely thankful to the IRTF staff for their commitment to the observation of 46P/Wirtanen during its historic 2018 apparition and for facilitating us in obtaining one of the richest data sets for the comet in the near-IR. The authors wish to recognize and acknowledge the very significant cultural role and reverence that the summit of Maunakea has always had within the indigenous Hawaiian community. We are most fortunate and grateful to have the opportunity to conduct observations from this mountain. N.D.R. and R.J.V. acknowledge support from the NASA Emerging Worlds Program under grant 80NSSC20K0341. D.Q. acknowledges support from NASA under award 80GSFC21M0002. M.R.C. and Y.S. acknowledge support from NASA under award 80NSSC20K0651. B.P.B. acknowledges support from NSF under award AST-2009398 and NASA Solar System Workings under award 80NSSC20K0651. E.G., and Y.K. acknowledge support from NSF under award AST-2009910.

ORCID iDs

Younas Khan https://orcid.org/0000-0003-4773-2674
Erika L. Gibb https://orcid.org/0000-0003-0142-5265
Nathan X. Roth https://orcid.org/0000-0002-6006-9574
Michael A. DiSanti https://orcid.org/0000-0001-8843-7511
Neil Dello Russo https://orcid.org/0000-0002-8379-7304
Boncho P. Bonev https://orcid.org/0000-0002-6391-4817
Mohammad Saki https://orcid.org/0000-0003-2277-6232
Ronald J. Vervack, Jr. https://orcid.org/0000-0002-8227-9564
Adam J. McKay https://orcid.org/0000-0002-0622-2400
Hideyo Kawakita https://orcid.org/0000-0003-2011-9159
Michael R. Combi https://orcid.org/0000-0002-9805-0078
Danna Qasim https://orcid.org/0000-0002-3276-4780

References

A'Hearn, M. F., Belton, M. J. S., Delamere, W. A., et al. 2011, Sci, 332, 1396
A'Hearn, M. F., Millis, R. L., Schleicher, D. G., Osip, D. J., & Birch, P. V. 1995, Icar, 118, 223
Altwegg, K., Balsiger, H., Bar-Nun, A., et al. 2015, Sci, 347, 1261952
Bergman, P., Lerner, M. S., Olofsson, A. O. H., et al. 2022, A&A, 660, A118
Biver, N., & Bockelée-Morvan, D. 2019, ESC, 3, 1550
Biver, N., Bockelée-Morvan, D., Boissier, J., et al. 2021, A&A, 648, A49
Biver, N., Bockelée-Morvan, D., Crovisier, J., et al. 1999, AJ, 118, 1850
Biver, N., Moreno, R., Bockelée-Morvan, D., et al. 2016, A&A, 589, A78
Bockelée-Morvan, D., & Biver, N. 2017, RSPTA, 375, 20160252
Bockelée-Morvan, D., Crovisier, J., Erard, S., et al. 2016, MNRAS, 462, S170
Bockelée-Morvan, D., Crovisier, J., Mumma, M. J., & Weaver, H. A. 2004, in Comets II, ed. M. C. Festou, H. U. Keller, & H. A. Weaver (Tucson, AZ: Univ. Arizona Press)
Bockelée-Morvan, D., Lis, D. C., Wink, J. E., et al. 2000, A&A, 353, 1101
Boehnhardt, H., Delahodde, C., Sekiguchi, T., et al. 2002, A&A, 387, 1107
Bonev, B. P. 2005, PhD thesis, Univ. Toledo, http://astrobiology.gsfc.nasa.gov/Bonev_thesis.pdf
Bonev, B. P., Dello Russo, N., DiSanti, M. A., et al. 2021, PSJ, 2, 45
Bonev, B. P., Mumma, M. J., DiSanti, M. A., et al. 2006, ApJ, 653, 774
Bonev, B. P., Mumma, M. J., Radeva, Y. L., et al. 2008, ApJL, 680, L61
Bonev, B. P., Mumma, M. J., Villanueva, G. L., et al. 2007, ApJL, 661, L97
Bonev, B. P., Villanueva, G. L., Paganini, L., et al. 2013, Icar, 222, 740
Bregman, J. D., Witteborn, F. C., Allamandola, L. J., et al. 1987, A&A, 187, 616
Cochran, A. L., Barker, E. S., & Gray, C. L. 2012, Icar, 218, 144
Combi, M. R., Harris, W. M., & Smyth, W. H. 2004, in Comets II, ed. M. C. Festou, H. U. Keller, & H. A. Weaver (Tucson, AZ: Univ. Arizona Press), 523
Combi, M. R., Lee, Y., Patel, T. S., et al. 2011, AJ, 141, 128
Combi, M. R., Mäkinen, T., Bertaux, J.-L., et al. 2020, PSJ, 1, 72
Combi, M. R., Mäkinen, T. T., Bertaux, J. L., et al. 2019, Icar, 317, 610
Contreras, C. S., & Salama, F. 2013, ApJS, 208, 6
Cordiner, M. A., Remijan, A. J., Boissier, J., et al. 2014, ApJL, 792, L2
Coulson, I. M., Liu, F.-C., Cordiner, M. A., et al. 2020, AJ, 160, 182
Cowan, J. J., & A'Hearn, M. F. 1979, M&P, 21, 155
Creswell, R. A., Winnewisser, G., & Gerry, M. C. L. 1977, JMoSp, 65, 420
Dello Russo, N., DiSanti, M. A., Magee-Sauer, K., et al. 2004, Icar, 168, 186
Dello Russo, N., DiSanti, M. A., Mumma, M. J., Magee-Sauer, K., & Rettig, T. W. 1998, Icar, 135, 377
Dello Russo, N., Kawakita, H., & Bonev, B. P. 2020, Icar, 335, 113411
Dello Russo, N., Kawakita, H., Vervack, R. J., Jr., & Weaver, H. A. 2016, Icar, 278, 301
Dello Russo, N., Vervack, R. J., Jr., Kawakita, H., et al. 2022, PSJ, 3, 6
Dello Russo, N., Vervack, R. J., Jr., Lisse, C. M., et al. 2011, ApJL, 734, L8
Dello Russo, N., Vervack, R. J., Jr., Weaver, H. A., et al. 2009, ApJ, 703, 187
Dello Russo, N., Vervack, R., Weaver, H., et al. 2007, Natur, 448, 172
DiSanti, M., Bonev, B., Dello Russo, N., et al. 2021, PSJ, 2, 225
DiSanti, M. A., Bonev, B. P., Dello Russo, N., et al. 2017, AJ, 154, 246
DiSanti, M. A., Bonev, B. P., Gibb, E. L., et al. 2016, ApJ, 820, 34
DiSanti, M. A., Bonev, B. P., Gibb, E. L., et al. 2018, AJ, 156, 258
DiSanti, M. A., Bonev, B. P., Magee-Sauer, K., et al. 2006, ApJ, 650, 470
DiSanti, M. A., Bonev, B. P., Villanueva, G. L., & Mumma, M. J. 2013, ApJ, 763, 1
DiSanti, M. A., Mumma, M. J., Dello Russo, N., & Magee-Sauer, K. 2001, Icar, 153, 361
DiSanti, M. A., Villanueva, G. L., Paganini, L., et al. 2014, Icar, 228, 167
Faggi, S., Mumma, M., Villanueva, G., Paganini, L., & Lippi, M. 2019, AJ, 158, 254
Faggi, S., Villanueva, G., Mumma, M., Paganini, L., et al. 2018, AJ, 156, 68
Farnham, T., Knight, M., Schleicher, D., et al. 2018, CBET, 4571, 1
Fink, U. 2009, Icar, 201, 311
Fink, U., Doose, L., Rinaldi, G., et al. 2016, Icar, 277, 78
Gibb, E. L., Bonev, B. P., Villanueva, G. L., et al. 2012, ApJ, 750, 102
Gibb, E. L., Mumma, M. J., Dello Russo, N., DiSanti, M. A., & Magee-Sauer, K. 2003, Icar, 165, 391
Gladman, B. 2005, Sci, 307, 71
Gomes, R., Levison, H. F., Tsiganis, K., & Morbidelli, A. 2005, Natur, 435, 466
Groussin, & Lamy 2003, A&A, 412, 879
Groussin, O., Lamy, P., Jorda, L., & Toth, I. 2004, A&A, 419, 375
Harker, D. E., Woodward, C. E., & Wooden, D. H. 2005, Sci, 310, 278
Hartogh, P., Lis, D. C., Bockelée-Morvan, D., et al. 2011, Natur, 478, 218
Hässig, M., Altwegg, K., Balsiger, H., et al. 2015, Sci, 347, aaa0276

Irvine, W. M., Schloerb, F. P., Crovisier, J., Fegley, B., Jr., & Mumma, M. J. 2000, in Protostars and Planets IV, ed. V. Mannings, A. P. Boss, & S. S. Russell (Tucson, AZ: Univ. Ariz. Press), 1159

Jehin, E., Moulane, Y., Manfroid, J., & Pozuelos, F. 2018, CBET, 4585, 1

Kawakita, H., Kobayashi, H., Dello Russo, N., et al. 2013, Icar, 222, 723

Kelley, M. S., Lindler, D. J., Bodewits, D., et al. 2013, Icar, 222, 634

Khan, Y., Gibb, E. L., Bonev, B. P., et al. 2021, PSJ, 2, 20

Knight, M. M., Schleicher, D. G., & Farnham, T. L. 2021, PSJ, 2, 104

Kobayashi, & Kawakita 2010, PASJ, 62, 1025

Lamy, et al. 1998, A&A, 335, L25

Lamy, P. L., Toth, I., A'Hearn, M. F., & Weaver, H. A. 1999, Icar, 140, 424

Läuter, M., Kramer, T., Rubin, M., & Altwegg, K. 2020, MNRAS, 498, 3995

Levison, H. F., & Duncan, M. J. 1997, Icar, 127, 13

Levison, H. F., Morbidelli, A., Tsiganis, K., Nesvorny, D., & Gomes, R. 2011, AJ, 142, 152

Lippi, M., Villanueva, G. L., DiSanti, M. A., et al. 2013, A&A, 551, A51

Lis, D. C., Bockelée-Morvan, D., Güsten, R., et al. 2019, A&A, 625, L5

Lis, D. C., Biver, N., Bockelée-Morvan, D., et al. 2013, ApJL, 774, L3

Lisse, C. M., Fernández, Y. R., Kundu, A., et al. 1999, Icar, 140, 189

Luspay-Kuti, A., Hässig, M., Fuselier, S. A., et al. 2015, A&A, 583, A4

Martin, E. C., Fitzgerald, M. P., McLean, I. S., et al. 2018, Proc. SPIE, 10702, 107020A

McKay, A. J., DiSanti, M. A., Cochran, A. L., et al. 2021, PSJ, 2, 21

Morbidelli, A., & Brown, M. E. 2004, in Comets II, ed. M. Festou, H. Keller, & H. Weaver (Tucson: Univ. Arizona Press), 175

Morbidelli, A., Levison, H. F., Tsiganis, K., & Gomes, R. 2005, Natur, 435, 462

Moulane, Y., Jehin, E., José Pozuelos, F., et al. 2019, EPSC, 13, 1036

Mumma, M. J., Bonev, B. P., Villanueva, G. L., et al. 2011, ApJL, 734, L7

Mumma, M. J., Weissman, P. R., & Stern, S. A. 1993, in Protostars and Planets III, ed. E. H. Levy & J. I. Lunine (Tucson: Univ. Ariz. Press), 1177

Nesvorný, D., Vokrouhlický, Dones, L., et al. 2017, ApJ, 845, 27

Paganini, L., Camarca, M. N., Mumma, M. J., et al. 2019, AJ, 158, 98

Paganini, L., Mumma, M. J., Boehnhardt, H., et al. 2013, ApJ, 766, 100

Protopapa, S., Sunshine, J. M., Feaga, L. M., et al. 2014, Icar, 238, 191

Protopapa, S., Kelley, M. S. P., Woodward, C. E., et al. 2021, PSJ, 2, 176

Qasim, D., Chuang, K.-J., Fedoseev, G., et al. 2018, A&A, 612, A83

Radeva, Y., Mumma, M. J., Villanueva, G. L., et al. 2013, Icar, 223, 298

Radeva, Y. L., Mumma, M. J., Bonev, B. P., et al. 2010, Icar, 206, 764

Rayner, J., Bond, T., Bonnet, M., et al. 2012, Proc. SPIE, 8446, 84462C

Rayner, J., Tokunaga, A., Jaffe, D., et al. 2016, Proc. SPIE, 9908, 990884

Roth, N. X., Boney, B. P., DiSanti, M. A., et al. 2021a, PSJ, 2, 54

Roth, N. X., Gibb, E. L., Bonev, B. P., et al. 2017, AJ, 153, 168

Roth, N. X., Gibb, E. L., Bonev, B. P., et al. 2018, AJ, 156, 251

Roth, N. X., Gibb, E. L., Bonev, B. P., et al. 2020, AJ, 159, 42

Roth, N. X., Milam, S. N., Cordiner, M. A., et al. 2021b, PSJ, 2, 55

Rubin, M., Altwegg, K., Balsiger, H., et al. 2019, MNRAS, 489, 594

Saki, M. 2021, PhD thesis, Univ. Missouri Saint Louis, https://irl.umsl.edu/dissertation/868/

Saki, M., Gibb, E. L., Bonev, B. P., et al. 2021, AJ, 162, 145

Schleicher, D. G. 2007, Icar, 190, 406

Schleicher, D. G., & Bair, A. 2014, in Proc. Asteroids Comets Meteors Conf., ed. K. Muinonen (Helsinki: Univ. Helsinki), 475

Snodgrass, C., Fitzsimmons, A., Lowry, S. C., & Weissman, P. 2011, MNRAS, 414, 458

Villanueva, G. L., DiSanti, M. A., Mumma, M. J., & Xu, L.-H. 2012a, ApJ, 747, 37

Villanueva, G. L., Magee-Sauer, K., & Mumma, M. J. 2013, JQSRT, 129, 158

Villanueva, G. L., Mumma, M. J., Bonev, B. P., et al. 2012b, JQSRT, 113, 202

Villanueva, G. L., Mumma, M. J., Bonev, B. P., DiSanti, M. A., & Gibb, E. L. 2009, ApJL, 690, L5

Villanueva, G. L., Mumma, M. J., DiSanti, M. A., et al. 2011a, Icar, 216, 227

Villanueva, G. L., Mumma, M. J., & Magee-Sauer, K. 2011b, JGRE, 116, 08012

Villanueva, G. L., Mumma, M. J., Novak, R. E., & Hewagama, T. 2008, Icar, 195, 34

Villanueva, G. L., Smith, M. D., Protopapa, S., Faggi, S., & Mandell, A. M. 2018, JQSRT, 217, 86

Wang, Z., Zhang, S.-B., Tseng, W.-L., et al. 2020, AJ, 159, 240

Weaver, H. A., Feldman, P. D., A'Hearn, M. F., et al. 2011, ApJ, 734, 5

Willacy, K., Turner, N., Bonev, B., et al. 2022, ApJ, 931, 164

Wooden, D. H., Woodward, C. E., & Harker, D. E. 2004, ApJL, 612, L77

Zolensky, M. E., Zega, T. J., Yano, H., et al. 2006, Sci, 314, 1735